


Summer 2014

Empirical Modeling of Asynchronous Scalp Recorded and Intracranial EEG Potentials

Komalpreet Kaur
Old Dominion University

Follow this and additional works at: https://digitalcommons.odu.edu/ece_etds

 Part of the [Bioelectrical and Neuroengineering Commons](#), [Computer Engineering Commons](#), and the [Electrical and Computer Engineering Commons](#)

Recommended Citation

Kaur, Komalpreet. "Empirical Modeling of Asynchronous Scalp Recorded and Intracranial EEG Potentials" (2014). Doctor of Philosophy (PhD), dissertation, Electrical/Computer Engineering, Old Dominion University, DOI: 10.25777/hmpg-x793
https://digitalcommons.odu.edu/ece_etds/93

This Dissertation is brought to you for free and open access by the Electrical & Computer Engineering at ODU Digital Commons. It has been accepted for inclusion in Electrical & Computer Engineering Theses & Dissertations by an authorized administrator of ODU Digital Commons. For more information, please contact digitalcommons@odu.edu.

**EMPIRICAL MODELING OF ASYNCHRONOUS SCALP
RECORDED AND INTRACRANIAL EEG POTENTIALS**

by

Komalpreet Kaur

B.S. May 2003, Guru Nanak Dev University, India
M.S. May 2006, PEC University of Technology, India

A Dissertation Submitted to the Faculty of
Old Dominion University in Partial Fulfillment of the
Requirement for the Degree of

DOCTOR OF PHILOSOPHY

ELECTRICAL AND COMPUTER ENGINEERING

OLD DOMINION UNIVERSITY

August 2014

Approved by:

Dean J. Krusienski (Director)

Jiang Li (Member)

Christian Zenlin (Member)

Frederic D. McKenzie (Member)

ABSTRACT

EMPIRICAL MODELING OF ASYNCHRONOUS SCALP RECORDED AND INTRACRANIAL EEG POTENTIALS

Komalpreet Kaur
Old Dominion University, 2014
Director: Dr. Dean J. Krusienski

A Brain-Computer Interface (BCI) is a system that allows people with severe neuromuscular disorders to communicate and control devices using their brain signals. BCIs based on scalp-recorded electroencephalography (s-EEG) have recently been demonstrated to provide a practical, long-term communication channel to severely disabled users. These BCIs use time-domain s-EEG features based on the P300 event-related potential to convey the user's intent. The performance of s-EEG-based BCIs has generally stagnated in recent years, and high day-to-day performance variability exists for some disabled users. Recently intracranial EEG (i-EEG), which is recorded from the cortical surface or the hippocampus, has been successfully used to control BCIs in experimental settings. Because these recordings are closer to the sources of the neural activity, i-EEG provides superior signal-to-noise ratio, spatial resolution, and broader bandwidth compared to s-EEG. However, because i-EEG requires surgery and the long-term efficacy for BCIs must still be explored, this approach is still not an option for patients. In order to improve s-EEG BCI performance, it is important understand the underlying brain phenomena and exploit the relationships between the s-EEG and generally superior i-EEG signals. Because the human head acts as a volume conductor consisting of the brain, cerebrospinal fluid, skull,

and scalp tissue, linear mathematical models can be used to relate s-EEG and i-EEG. This dissertation presents unique s-EEG and i-EEG data that were recorded from the same subjects and used to develop novel empirical models to estimate s-EEG from i-EEG. These new empirical models can be used to better understand the sources and propagation of the relevant neural activity, as well as to validate existing theoretical volume conduction models. It is envisioned that this knowledge will help to advance algorithms for improving s-EEG BCI performance.

This work is dedicated:

To the Almighty

To my mother, Mrs. Harbhajan Kaur, for her constant motivation and prayers.

To my father, Mr. Harbhajan Singh, for having faith in me.

To my husband, Dr. Manish Wadhwa, for his constant support and encouragement.

To my brother, Mr. Amandeep Singh, for always standing by my side.

ACKNOWLEDGEMENTS

Any work without acknowledging the people that make it a success is incomplete. First, I would like to thank my advisor, Dr. Dean J. Krusienski, for giving me guidance and counsel from time to time throughout this process. Without his able guidance I would not have succeeded in this endeavor. His constant motivation and feedback helped me at every step. I thank him for being always willing to help me whenever I approached him.

I would like to thank Dr. Demetrios Voreades and Dr. Mark Pflieger from Source Signal Imaging, Inc. for providing me with the EMSE Suite and helping me with the source localization based data analysis.

I am grateful to my dissertation committee members, Dr. Jiang Li, Dr. Christian Zemlin, and Dr. Frederic D. McKenzie, for their help, comments, and suggestions.

I thank my friend, Shreya Chakrabarti, for always being there as a friend and support away from home. I thank all my labmates who have directly or indirectly participated in making this a success.

TABLE OF CONTENTS

	Page
LIST OF TABLES	ix
LIST OF FIGURES	xiii
 Chapter	
1. INTRODUCTION	1
1.1 BRAIN COMPUTER INTERFACE	2
1.2 P300 RESPONSE	4
1.3 MOTIVATION	8
1.4 DISSERTATION CONTRIBUTIONS AND OUTLINE	10
2. ELECTROENCEPHALOGRAM	11
2.1 SCALP ELECTROENCEPHALOGRAM	11
2.2 INTRACRANIAL ELECTROENCEPHALOGRAM	17
2.3 DATA COLLECTION	18
3. DIRECT MODEL	25
3.1 MODELING SCALP ELECTROENCEPHALOGRAM USING INTRACRA- NIAL ELECTROENCEPHALOGRAM	25
3.2 DIRECT MODEL WITH CHANNEL SELECTION	28
4. DIRECT MODELS WITH SPATIAL FILTERING	35
4.1 DIRECT MODEL WITH PRINCIPAL COMPONENT ANALYSIS	36
4.2 DIRECT MODEL WITH INDEPENDENT COMPONENT ANALYSIS ..	40
4.3 DIRECT MODEL WITH STATIONARY SUBSPACE ANALYSIS	45
4.4 COMPARISON	50
5. PERFORMANCE-BASED MODEL	53
5.1 PERFORMANCE-BASED MODEL	54
5.2 DISCUSSION	59
6. SOURCE-BASED MODEL	61
6.1 SOURCE LOCALIZATION	61
6.2 SOURCE LOCALIZATION FOR INTRACRANIAL EEG	68
6.3 SOURCE-BASED MODEL	73
7. DISCUSSION, CONTRIBUTIONS, AND FUTURE DIRECTIONS	79
7.1 DISCUSSION	79
7.2 CONTRIBUTIONS	82
7.3 FUTURE DIRECTIONS	83

REFERENCES 85

APPENDIX 93

VITA 95

LIST OF TABLES

Table	Page
I. Classification accuracies for s-EEG and i-EEG for six subjects.	24
II. Classification Accuracies for Direct model with channel selection. Columns two and three correspond to the optimal linear classifier derived from the s-EEG and iEEG data. The fourth column gives the classification accuracies from Direct model with channel selection.	33
III. Classification accuracies for Direct models. Columns two and three correspond to optimal linear classifier derived from the s-EEG and iEEG data. The fourth column gives the results from Direct model with channel selection. The fifth, sixth and seventh columns give the classification accuracies from Direct model using PCA, ICA, and SSA, respectively.	51
IV. Classification accuracies for Direct model (with channel selection) and Performance-based model. Columns two and three correspond to optimal linear classifier derived from the s-EEG and iEEG data. The fourth and fifth columns give the results from Performance-based model and Direct model (with channel selection), respectively.	57

LIST OF FIGURES

Figure	Page
1. Basic Block Diagram of a BCI System. The brain signals are measured by the electrodes and then amplified. Appropriate features are extracted from the acquired signals that reflect the user's intent. These features are classified into logical controls by the feature translator. These device commands operate a device [3].	3
2. Average P300 Response for channel Cz for Subject C. The blue waveform represents the Target ERP while the red corresponds to the Non-target ERP.	5
3. The 6×6 matrix containing alphabets and numbers. Different rows and columns of the matrix are flashed randomly.	6
4. Four sphere head model consisting of Cortex, CSF, Skull and Scalp [32](used with permission).	9
5. Recording sites for electrophysiological signals. A: Scalp EEG is recorded by placing the electrodes on the scalp B: ECoG is recorded by placing the electrodes on the cortical surface C: LFPs are recorded by micro electrodes arrays inserted in the cortex [32] (used with permission).	12
6. 10 – 20 International System used for placement of scalp electrodes [34]. For this international standard, the distances between adjacent electrodes are either 10% or 20% of the total frontback or rightleft distance of the skull.	14
7. Location of Intracranial electrodes (red ones show the electrodes that were used for recording). Different subjects had different numbers of electrodes and locations of i-EEG depending on the clinical requirement.	20
8. The 6×6 matrix used in this dissertation. A row or column intensifies for 100 ms every 175 ms. The letter in the parentheses at the top of the window is the current target letter "D". For this target, a P300 should be elicited when the fourth column or first row is intensified [39].	21
9. Direct ERP Modeling Block Diagram. A linear combination of i-ERPs are used to model each s-ERP independently using ordinary least square regression.	27
10. Root Mean Square Error obtained between archetype ERPs and modeled ERPs using the direct modeling approach.	28

11. s-EEG single channel accuracies (SCA) topographies for the six subjects (A-F). Black dots represent the fixed 32-channel electrode positions according to the International 10-20 system [34]. SCA was determined using the ERP amplitude features from a single channel to derive the respective channel's classifier based on [39]. 29
12. iEEG single channel accuracies (SCA) topographies for the six subjects (A-F). For each subject, iEEG SCA topographies are plotted on generic brain models with electrode locations indicated by the circles. The black circles represent the electrodes that were used for the BCI recordings and modeling, whereas white electrodes were only used for clinical recordings and not represented in the models. 30
13. Direct modeling block diagram with optimally selected iEEG channels. A linear combination of the optimally selected iERPs are used to model each s-ERP independently using ordinary least squares regression. 31
14. ERPs and Spatial models for Direct model. The first column shows the three iERPs for each subject (A-F) corresponding to channels with the highest SCA, with red representing the highest SCA and blue representing the second highest SCA. The second column shows the RMSE topographies, with the channel corresponding to the lowest RMSE circled in purple and channel Cz circled in green. The third and fourth columns show the modeled ERPs and the corresponding spatial models, respectively, for the channel with the lowest RMSE. The fifth and sixth columns show the modeled ERPs and the corresponding spatial models for channel Cz. The channel weights for the spatial models were normalized to have a maximum magnitude of 1. 32
15. Schematic Diagram showing the Direct ERP based Model with Spatial Filter . 38
16. ERPs and Spatial models for Direct model with PCA. The first column shows the RMSE topographies for all the subjects with the lowest RMSE channel (i.e. 1st channel) circled in purple and channel Cz circled in green. The second and third columns show the Modeled and Archetype s-ERPs and the corresponding spatial models for the 1st channel. The fourth and fifth columns show the Modeled and Archetype s-ERPs and the spatial models for channel Cz. The channel weights for the spatial models were normalized to have a maximum magnitude of 1. 39

17. ERPs and Spatial models for Direct model with ICA. The first column shows the RMSE topographies with the channel corresponding to the lowest RMSE circled in purple, termed as 1st channels and channel Cz circled in green. The second and third columns show the Modeled and Archetype s-ERPs and the spatial models for the 1st channel. The fourth and fifth columns show the Modeled and Archetype s-ERPs and the spatial models for channel Cz. The channel weights for the spatial models were normalized to have a maximum magnitude of 1. 44
18. Schematic Diagram showing the Direct model with Stationary Subspace Analysis 48
19. ERPs and RMSE for Direct model with SSA. The first column shows the RMSE topographies with the channel corresponding to the lowest RMSE (1st channel) circled in purple and channel Cz circled in green. The second and third columns show the Modeled and Archetype ERPs and spatial weights for the first channel. The fourth and fifth columns show the Modeled and Archetype ERPs and spatial weights for the Cz channel. 49
20. Performance based modeling approach block diagram. The optimal spatial model is determined by minimizing the output error of the classifier. An ordinary least square linear regression is used to solve for the spatial weights in the linear system created by the cascade of the spatial model with the fixed s-ERP derived linear classifier. 54
21. Spatial models for performance-based modeling. The first column shows the s-EEG SCAs for each subject (A-F). The channels that were included in the s-EEG derived classifier are represented by black dots and the excluded channels as white dots. Additionally, the channel that was included in the s-EEG derived classifier having highest SCA is circled green (Top Model), the channel that was included in the s-EEG derived classifier having lowest SCA is circles in orange (Last Model) and the channel Cz is circled in magenta. The second through fourth columns show the spatial filters corresponding to the Top Model, Last Model and Cz, respectively. The last model is presented to illustrate how the iEEG contributes to the s-EEG channels that do not appear to contain much discriminative information in isolation, but can benefit the classifier in conjunction with other channels. 58
22. Schematic representation of the Source Localization 62
23. Axial, Coronal, and Sagittal views of FEM model for Subject C showing the white and gray matter. 69
24. Sources generated from LORETA for Subject C for i-EEG. Yellow circles represent the i-EEG electrode locations. 70

25.	Sources generated from LORETA for Subject E for i-EEG. Yellow circles represent the i-EEG electrode locations.	71
26.	Sources generated from LORETA for Subject A for i-EEG. Yellow circles represent the i-EEG electrode locations.	72
27.	Sources generated from LORETA for Subject B for i-EEG. Yellow circles represent the i-EEG electrode locations.	73
28.	Sources generated from LORETA for Subject D for i-EEG. Yellow circles represent the i-EEG electrode locations.	74
29.	Sources generated from LORETA for Subject F for i-EEG. Yellow circles represent the i-EEG electrode locations.	74
30.	Axial, Coronal, and Sagittal views of the FEM Head model for Subject C. The brown color represents the head, blue corresponds to the outer skull, inner skull is represented by yellow color, red is for the gray matter and green corresponds to the white matter of the head.	76
31.	ERPs and RMSE for Source-based Model. The first column shows the RMSE topographies with the channel corresponding to the lowest RMSE (first channel) circled in purple and channel Cz circled in green. The second and third columns show the Modeled and Archetype s-ERPs and spatial weights for the first channel. The fourth and fifth columns show the Modeled and Archetype s-ERPs and spatial weights for the Cz channel.	77

CHAPTER 1

INTRODUCTION

More than 2 million people in the US suffer from various neuromuscular disorders like amyotrophic lateral sclerosis (ALS), brainstem stroke, spinal cord injury, cerebral palsy, muscular dystrophia, multiple sclerosis etc. About 20,000 – 30,000 people in the US have ALS and approximately 5,600 people are diagnosed with ALS each year [1]. Each year 750,000 people in the US experience a stroke and 11,000 suffer from a spinal cord injury. 500,000 Americans currently live with cerebral palsy and 270,000 with multiple sclerosis [2].

These neural disorders affect the muscles or neural pathways that control muscles. In particular, patients with spinal cord injuries or ALS lose voluntary muscle control. Many patients may still retain some voluntary control of their facial muscles, which can be used as a reliable trigger for communication or control of some external device. However, in some severely affected patients, the disease can progress to a point that will cause “locked-in” syndrome. The patients in locked in syndrome are awake and fully aware but cannot communicate with the outside world due to complete paralysis [3]. Conventional assistive devices require some level of voluntary muscle control and thus are not appropriate for people in this condition [4].

In cases of severely affected patients, a Brain-Computer Interface (BCI) has the potential to establish a communication channel directly from the patient’s brain signals to the

This dissertation follows the style of *IEEE Transactions*.

computer. The signals recorded from the brain should be such that patients can reliably and voluntarily control an external system without any muscle movement. A BCI system provides an alternate pathway to convey messages and commands to the external world. BCI systems can replace, restore, enhance, supplement or improve the brain's natural interactions with its external and internal environment [3].

1.1 BRAIN COMPUTER INTERFACE

A BCI is a system that provides an alternative pathway to people with severe neuromuscular disorders to communicate with the outside world and control devices using their brain signals directly [3]. Rather than depending on the body's normal output pathways of nerve cells and muscles, the input control signals are represented by electrophysiological activity recorded from the brain.

BCI systems consist of four general components, namely: signal acquisition, feature extraction, feature translation, and device output. The signal acquisition involves the recording of neurological signals using various modalities such as scalp or intracranial Electroencephalography (EEG), Magnetoencephalography (MEG), functional Magnetic Resonance Imaging (fMRI), etc. The acquired signals are generally of very low amplitude, thus are amplified by a bio-signal amplifier, and digitized for further processing. Different methods of recording brain signals can be compared in terms of temporal and spatial resolution. Figure 1 gives the basic block diagram showing the components of a BCI system.

BCI systems can be broadly classified into invasive and non-invasive systems. Invasive BCI systems employ insertion of electrodes below the skull, often on the surface of the

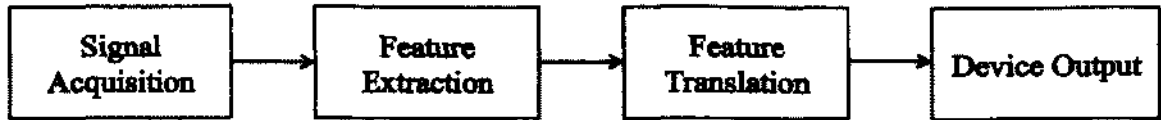


Fig. 1: Basic Block Diagram of a BCI System. The brain signals are measured by the electrodes and then amplified. Appropriate features are extracted from the acquired signals that reflect the user's intent. These features are classified into logical controls by the feature translator. These device commands operate a device [3].

brain [5] [6], or deep within the cortex [7] to record the brain signals. Non-invasive BCI systems involve measurements of electro-magnetic potentials from outside of the skull.

Non-invasive techniques of recording the brain signals do not involve any surgery or any significant risk. These techniques include fMRI, MEG and scalp Electroencephalography (s-EEG). MEG, PET, fMRI and MRI are robust but bulky and expensive systems that are generally not practical for BCI systems. Thus, these systems are not very popular for BCI systems. The techniques PET and fMRI depend on the blood flow, have long time constants, and thus are not very useful for rapid communication.

Invasive techniques for acquiring brain signals implant micro-electrodes into or in close proximity to the brain. Thus, these techniques provide good signal quality, temporal and spatial resolution. Electrocorticography (ECoG) is a method of implanting electrodes directly over the cortex that is routinely used for epilepsy monitoring and BCI research.

Currently, electrophysiological signals such as scalp EEG, ECoG, stereotactic depth electrodes [8] [9], and single neuron recordings appear to be the most promising and practical systems for BCI. This is because they have high temporal resolution and do not require bulky and expensive equipment.

Feature extraction is the process of extracting the features from the acquired brain signals that are related to the user's intent or mental state. The acquired brain signals generally suffer from low signal-to-noise ratio (SNR) and artifacts thus feature extraction algorithms attempt to represent the data in a more usable form. The most commonly extracted features used for BCI are time-triggered signal amplitudes and latencies, power within specific frequency bands or firing rates of individual cortical neurons.

Feature translation algorithms convert the extracted features into appropriate commands for the output device. A wide variety of regression models and classifiers can be used for feature translation. The output of the feature translation algorithm can be used to control augmentative peripheral devices such as virtual keyboard spellers, neuroprosthetics, motorized wheelchairs, etc.

1.2 P300 RESPONSE

One of the most commonly used signals for s-EEG BCI control is the P300 event-related potential (ERP). The P300 is produced in the brain when a rare or novel sensory stimulus is given. The P300 response is elicited by the "oddball" paradigm in which repeated stimuli are presented to the user. There is a specific target stimulus that rarely occurs among the more frequent non-target stimuli. Each time the target stimulus is presented a P300 response is elicited. The P300 response is characterized by a large positive deflection starting about 300 ms after the onset of the stimulus as shown in Figure 2, but the actual latency of the P300 can vary from 250 ms to 750 ms. This figure shows averaged target and non-target ERPs for one of the channel for a single subject. The blue waveform corresponds to the target P300 ERP and the red one corresponds to non-target P300 ERP.

As can be seen from Figure 2, a large positive deflection is observed between 200 and 300 ms after the stimulus. The amplitude of the P300 varies directly with the relevance of the eliciting events and inversely with the probability of the stimuli. P300 responses can be elicited by different sensory stimuli such as auditory stimuli [10] or visual stimuli [11]. The experimental protocol used for recording the data for the dissertation was based on the visual P300 speller paradigm.

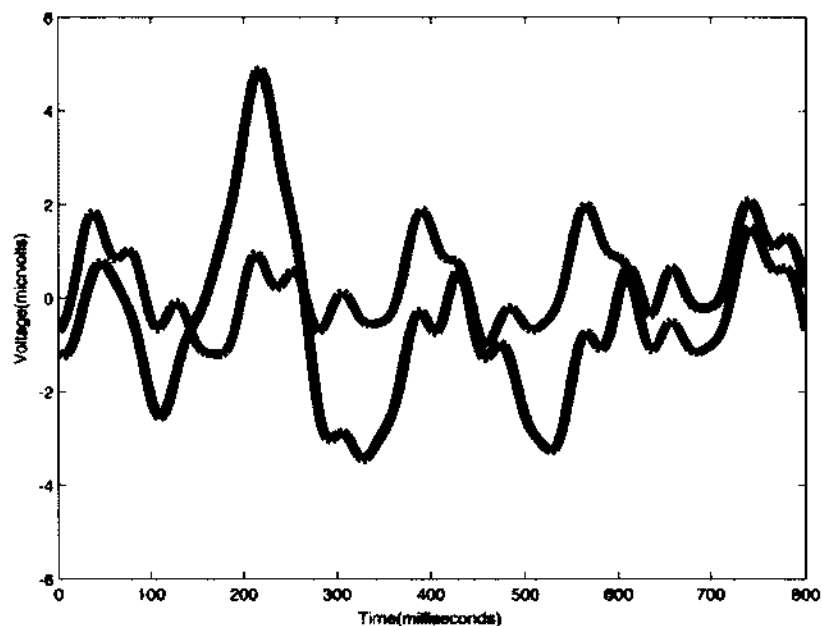


Fig. 2: Average P300 Response for channel Cz for Subject C. The blue waveform represents the Target ERP while the red corresponds to the Non-target ERP.

1.2.1 P300 SPELLER PARADIGM

Farwell and Donchin [12] [13] were the first to use P300 response to control a BCI that allows the user to type a single letter at a time, referred to as the P300 Speller. The P300 speller they developed consisted of a 6×6 matrix of letters and a few one word commands displayed on a CRT screen. Figure 3 shows the 6×6 matrix used for this dissertation.

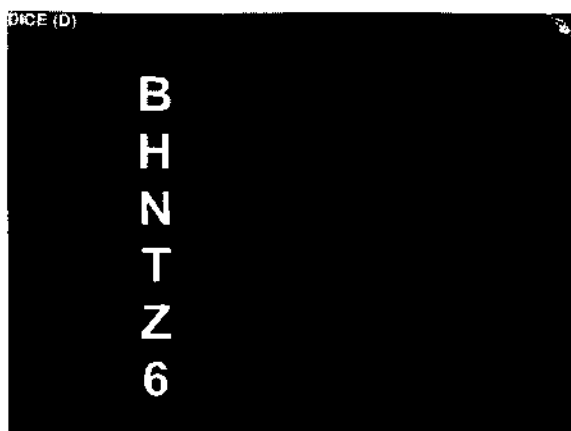


Fig. 3: The 6×6 matrix containing alphabets and numbers. Different rows and columns of the matrix are flashed randomly.

The rows and columns of the matrix flash randomly at a constant rate. The users are asked to focus attention on the letter (called a target) that they want to type and mentally count the number of times the target letter flashes. In response to the counting of this odd-ball stimulus, the desired row or column containing the target letter elicits a P300 response. A classifier is used to identify the target letter from the resulting ERPs. Recognition of the target letter is equivalent to finding the target row and column. Thus, a classifier detects the desired row and column at the intersection of which is the target letter.

A literature review of the field does not show any single P300 detection system to be the state of the art. Since s-EEG is a non-invasive method of recording the brain signals, s-EEG based P300 spellers have been studied extensively. For both online and offline experiments, a large variety of classification algorithms have been developed e.g. Peak Picking, Neural Networks, Stepwise Linear Discriminant Analysis (SWLDA)[14, 15]. Kaper, et al., [16] used a straightforward approach with Gaussian support vector machines (SVMs) to achieve perfect results with 5 averaged trials. Krusienski, et al., [14] reported the results of

a comparison of different classification algorithms, which showed that SWLDA and SVM perform well compared to other classifiers. Apart from varying the different classification algorithms, researchers have studied the effect of inter-stimulus interval (ISI) [17, 18] and matrix size [17] on the classification accuracy. Apart from using the standard P300 Speller where rows and columns of the matrix flash randomly, called row column paradigm (RCP), literature shows that different paradigms have been developed to improve the classification accuracy and speed. Some examples include a checkerboard paradigm developed by Townsend, et al., [19], the a rapid serial visual presentation (RSVP) paradigm proposed by Acqualagna and Blankertz [20], and the face speller proposed by Kaufmann, et al., [21] which consisted of flashing faces of famous individuals for items in the matrix. In all these paradigms, an increase in classification accuracy was obtained. Effects of variation in character size, inter character distance, background color, and chromatic differences in the flashing pattern on the P300 speller classification accuracy and speed have also been studied in detail.

The real test of a BCI is to validate the online performance with actual patients. Most P300 Speller implementations remain slow and impractical for disabled users. Some initial studies have been performed on amyotrophic lateral sclerosis (ALS) patients [22, 23] that show the P300 Speller can be used by this patient population. Using three ALS patients, Sellers and Donchin [22] used a simplified P300 BCI to select between only four choices. The results showed that two of the ALS patients were able to achieve offline accuracies comparable to the control group of able bodied subjects. Nijboer, et al., [23] found that four ALS patients with severe paralysis were able to achieve a mean offline accuracy of 79%

using P300 speller interface. These studies are promising and indicate that P300 speller is a viable option for text communication for severely disabled patients. Considerable variation in the day to day performance of a P300 based BCI has been observed in individuals with ALS [24, 25].

Although the P300 speller has been studied extensively and is one of the well established BCI systems, a recent review by Mak, et al., [26] concludes that more work still needs to be done to optimize speed, accuracy and reliability. The general BCI research community believes that a better understanding of the underlying neuroscience and neurophysiology can further improve the performance. Most of the P300 speller studies have used non-invasively recorded s-EEG. Recently, ECoG electrodes implanted on the cortex and stereotactic depth electrodes implanted in the hippocampus were used to control the P300 speller [27, 6, 28]. Since these electrodes are closer to the brain, they offer higher SNR, superior spatial resolution and broader bandwidth compared to s-EEG.

1.3 MOTIVATION

The human head acts as a volume conductor for the brain's electrical activity [29]. There are several mathematical and geometrical models of the human head as a volume conductor [30] [31]. These volume conduction models consider the human cranium to consist of brain (white matter and cortex), cerebrospinal fluid (CSF), skull, and scalp, as shown in Figure 4. Different layers have different conductivities and thickness. Skull tissue has low conductivity and thus the currents generated in the cortical region spread widely on reaching the scalp. Figure 4 represents different layers of the human head.

It is possible that scalp-recorded EEG (s-EEG) can be mathematically modeled as a

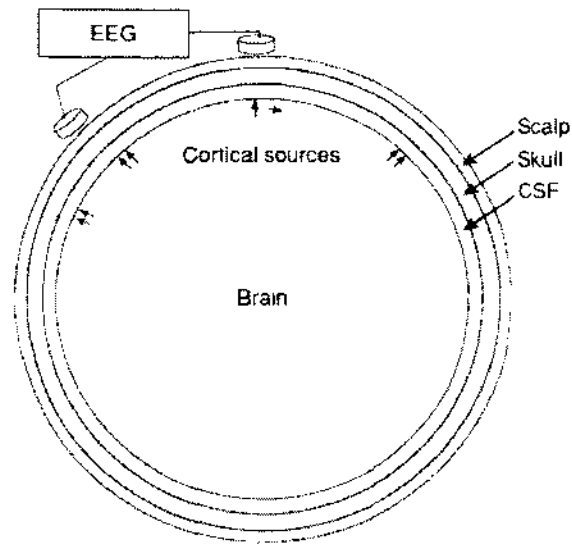


Fig. 4: Four sphere head model consisting of Cortex, CSF, Skull and Scalp [32](used with permission).

mixture of the underlying intracranially-recorded EEG (i-EEG). These models between s-EEG and i-EEG will help researchers better understand the electrical distribution, propagation and attenuation of the skull and scalp layers, and generally give a better idea about the underlying neurophysiology. This better understanding of the brain's phenomena is envisioned to pave the way for the development of more effective BCI processing techniques for improving s-EEG BCI performance.

For this dissertation, linear empirical models establishing a relationship between the scalp and intracranial EEG were developed. Firstly, direct models based on minimization of ERP modeling error were developed. Direct models with the addition of spatial filtering were then explored. A new optimization criteria based on BCI performance is introduced for the performance-based models. Lastly, source localization approaches were performed

to better understand the the relationship between the empirical models and existing theoretical models of conductivity. The estimated sources were used to develop a source-based model.

1.4 DISSERTATION CONTRIBUTIONS AND OUTLINE

The remainder of this dissertation is organized as follows. Chapter II discusses the electroencephalogram, both invasive and noninvasive methods of recording the EEG. This chapter also presents the details of the data used for this dissertation. This dissertation makes three major contributions towards modeling the relationship between the scalp and intracranial EEG. The three models developed in this direction are the direct model, performance-based model, and source-based model. Chapter III presents the first key contribution of this dissertation, direct model for modeling the s-EEG in terms of the i-EEG. The developed models can accurately estimate the scalp ERP waveform morphologies from the underlying intracranial ERPs. Chapter IV considers various spatial filtering techniques to improve the direct models. Three spatial filtering techniques, namely Principal Component Analysis (PCA), Independent Component Analysis (ICA), and Stationary Subspace Analysis (SSA), are evaluated. Chapter V proposes the second key contribution of this dissertation by introducing a novel performance-based model to relate s-EEG and i-EEG. BCI performance based on P300 classification accuracy is considered for developing the model. Chapter VI presents the third key contribution of this dissertation, a novel source-based model that uses the sources estimated from i-EEG to estimate s-EEG. Chapter VII concludes by summarizing the important components of this dissertation and presenting areas of future work.

CHAPTER 2

ELECTROENCEPHALOGRAM

Electrophysiological signals like the scalp electroencephalogram (EEG), electrocorticogram (ECoG), and local field potentials (LFPs) are most commonly used for BCI systems. These electrophysiological signals have high temporal resolution, which is needed for rapid communication using BCI. Scalp-electroencephalographic electrodes are attached to the skin to record the field potentials from very large and widely distributed sets of underlying neurons and synapses. ECoG electrode arrays are surgically positioned on the brain surface to record field potentials from smaller, more localized sets of neurons and synapses. LFPs are recorded from microelectrode arrays surgically inserted into the cerebral cortex to record neuronal action potentials from individual neurons or small, highly localized sets of neurons and synapses. Figure 5 shows the different recording sites for electrophysiological signals.

In this dissertation, i-EEG is used to describe both ECoG on the cortex and stereotactic depth electrodes in the hippocampus, which both have similar contact dimensions. Different models are developed for establishing the relationship between the scalp EEG and intracranial EEG referred to as s-EEG and i-EEG, respectively.

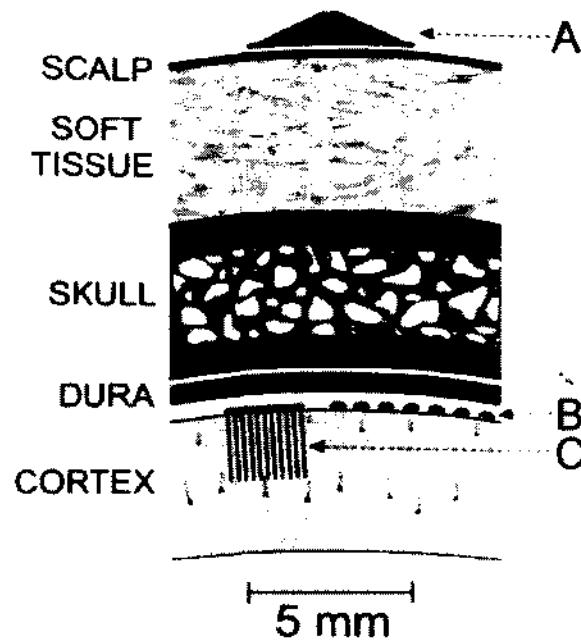


Fig. 5: Recording sites for electrophysiological signals. A: Scalp EEG is recorded by placing the electrodes on the scalp B: ECoG is recorded by placing the electrodes on the cortical surface C: LFPs are recorded by micro electrodes arrays inserted in the cortex [32] (used with permission).

2.1 SCALP ELECTROENCEPHALOGRAM

s-EEG is the most popularly used method for acquiring brain signals for BCI systems. It is noninvasive, safe and relatively inexpensive. The electric potentials are measured by placing the electrodes on the scalp using passive or active electrodes. Conductive gel is generally applied between the electrodes and skin to improve conductivity. Passive electrodes are simply metal disks connected to an amplifier by a cable. Since the brain signal amplitudes are generally very low, they are more susceptible to contamination by movements of the cable and other environmental noises. Alternatively, active electrodes have a preamplifier inside the electrode. Thus, these electrodes are less prone to environmental noise but more expensive than passive electrodes [33].

s-EEG signals typically have an amplitude of 10-20 μV , spatial resolution on a scale of centimeters, and spectral bandwidth of 0-70 Hz [33]. The original potential at the cortical surface is about 1.5 μV , but it gets attenuated by the cerebrospinal fluid, dura matter, bone, scalp etc. when it reaches the scalp. Thus the recorded s-EEG must be amplified using a bio-signal amplifier. Also, the signal recorded is analog so it must be converted to a digital signal so that further processing can be done on the acquired signal. The amplified s-EEG signals are passed through an Analog to Digital Converter (ADC) with a sufficient sampling rate (e.g., typically 80-200 Hz for s-EEG).

To allow exchange and interpretation of data across laboratories and to have uniformity in nomenclature, the International Federation in Electroencephalography and Clinical Neurophysiology adopted a standard in 1958 for electrode placement called the 10 – 20 *Placement System* [34]. Even today, it is the most commonly used system. This system standardizes the physical locations and designations of the electrodes to be placed on the scalp. This system is based on an iterative subdivision of arcs on the scalp starting from particular reference points on the skull: Nasion (Ns), Inion (In), and Left and Right Pre-Auricular points (PAL and PAR respectively). The intersection of the longitudinal (Ns-In) and lateral (PAL-PAR) diagonals is called the vertex. This system divides the head into proportional distances (called 10 – 20 percentages) from the reference points. Electrodes are designated according to adjacent brain areas: F (Frontal), C (Central), T (Temporal), P (Parietal), and O (Occipital). These letters are accompanied by odd numbers for electrodes on the left side of the head and even numbers for electrodes on the right side of the head. Figure 6 shows the standard 10 – 20 system.

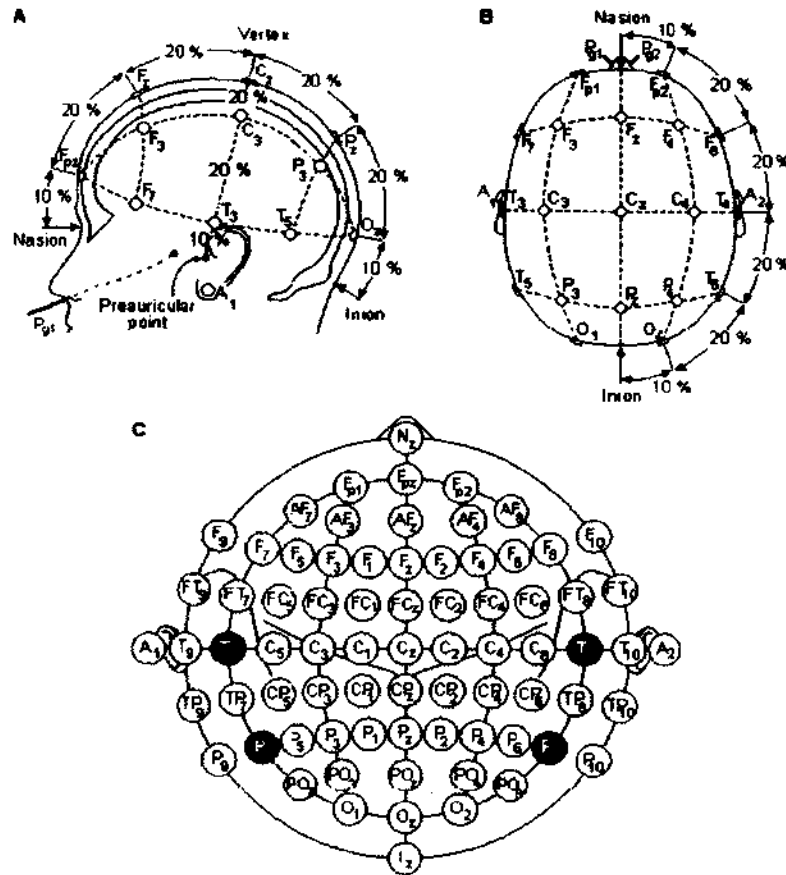


Fig. 6: 10 – 20 International System used for placement of scalp electrodes [34]. For this international standard, the distances between adjacent electrodes are either 10% or 20% of the total frontback or rightleft distance of the skull.

Electrophysiological Features Detected by s-EEG

Using modern signal acquisition methods, the signal-to-noise ratio of s-EEG is very low above around 40 Hz. For clinical purposes, frequencies between 0.3 to 80 Hz are typically used. This spectrum is further divided into different frequency sub bands:

Delta Rhythm (upto 4 Hz): This subband has highest amplitude. These rhythms are most prominent in normal children during the first year of life, but may appear in posterior region throughout maturation. These also occur during deep sleep.

Theta Rhythm (4 – 8 Hz): This rhythm is a low amplitude irregular rhythm and a usual feature present in the s-EEG of a normal awake adult. This is found in locations not related to any task but are prominent in states of drowsiness and sleep.

Alpha Rhythm (8 – 13 Hz): This rhythm occurs during wakefulness over the posterior region on the head, generally with a higher voltage over the occipital areas. It is best seen when the eyes are closed and in a physically relaxed state.

Mu Rhythm (8 – 13 Hz): This rhythm overlaps with alpha rhythm. It reflects the synchronized firing of neurons over the motor cortex in a resting state.

Beta Rhythm (13 – 30 Hz): This rhythm occurs in sensorimotor cortex. It is linked to the motor behavior and is attenuated during active movements.

Gamma Rhythm (26 – 100 Hz): This is a very high frequency activity associated with perception and consciousness. It is observed during higher mental tasks like perception, learning and memory [35].

s-EEG recordings can be contaminated by artifacts that may result from power line interference, patient movement, or other electrical sources. These artifacts can lead to misinterpretation of the underlying brain activity. Some commonly occurring artifacts are as follows:

1. **Electromagnetic Induction:** Since s-EEG voltages are of very low amplitude, they can be easily contaminated by electromagnetic influences. The power supply lines use a sinusoidal voltage with a frequency of 50 or 60 Hz. Mains interference is ubiquitous in s-EEG recordings. Most bio-signal amplifiers have a notch filter that suppress signals in a narrow band around the power line frequency.

2. **Eye Movement and Blinking Artifacts:** The front of an eye ball has a positive potential with respect to its back. Therefore, the eye creates a dipole and movements of the eye ball can affect scalp potential. Eyeblink artifacts are generated by fast movements of the eyelid along the cornea. This friction between lid and cornea results in charge separation. In s-EEG this effect is recorded as a positive peak that lasts a few tenths of a second, most prominent in the prefrontal region, but propagates to all the electrodes of the montage. Ocular artifacts (Electrooculogram or EOG) are produced by eye movements, because of the frictional mechanism between retina and cornea. Electrodes are applied left and right or above and below the eyes to record the variations in the electrical potentials. This artifact can be excluded by subtracting the weighted EOG signal from the scalp electrodes or using Independent Component Analysis (ICA).
3. **Muscular Artifacts:** Muscle movements can also be picked up on the scalp and are called Electromyogram (EMG). These are produced due to the movement of facial or scalp muscles like shivering, smiling, lifting the eyebrows, chewing, or grinding of teeth. On s-EEG, these artifacts are observed as bursts of high frequency activity superimposed on low frequency waves. This artifact can hide the underlying cerebral activity. The frequency distribution of EMG artifacts is very broad. Thus, they affect the amplitude of mu/beta rhythms.
4. **Cardiac Activity or Electrocardiogram (ECG):** ECG artifacts can also be observed in s-EEG. Since the electric potential of the heart is equipotential on the

scalp, ECG may not be picked up in bipolar recordings. But with a common reference, ECG can appear periodically on s-EEG [35].

Although the SNR of s-EEG is low, because of its non-invasive nature, it has been studied extensively in humans, and its characteristics and capabilities for BCI are very well established.

2.2 INTRACRANIAL ELECTROENCEPHALOGRAM

Electrocorticography (ECoG) is an invasive technique of recording the electrical signals from locations under the skull but not within the brain. These can be recorded by placing the electrodes on the surface of the dura mater (*epidurally*) or using screws that penetrate the skull and act as electrodes. ECoG can also be recorded from beneath the dura mater (*subdurally*) by placing the electrodes directly on the surface of the brain. ECoG electrodes are in the form of an array (e.g. 8×4 electrodes) or strip (e.g. 1×8 electrodes) having an inter electrode distance of 5 – 10 mm. These are usually implanted in humans to localize epileptic seizure foci. These are generally implanted for 1 – 2 weeks. Apart from ECoG electrodes, Stereotactic Depth macro Electrodes (SDEs) are also implanted to localize seizures in patients with epilepsy. SDEs improve the risk/benefit ratio for chronic intracranial implantation compared to ECoG with grid electrodes [7]. ECoG and SDEs are commonly referred to as Intracranial Electroencephalography (i-EEG). The configuration and location of the electrodes and duration of the implant is determined solely by clinical requirements and without any regard to research needs.

Since i-EEG electrodes are placed under the skull and are close to the cortical surface, they can detect brain activity more accurately. i-EEG offers several advantages compared to s-EEG. i-EEG has higher spatial resolution (1.4 mm), higher amplitude (50 – 100 μ V), is less vulnerable to artifacts and has broader bandwidth (0 – 500 Hz) [36] [5]. i-EEG detects a number of physiological phenomena that are represented in different time or frequency domain components and their interactions, e.g. mu/beta rhythms, gamma activity. i-EEG-based BCIs provide control comparable or even superior to that reported for s-EEG based BCIs [37].

i-EEG signals offer higher SNR as compared to s-EEG, but suffer from the limitation that these are implanted in specific patient groups (e.g. intractable epilepsy) prior to brain surgery. Thus, the frequency of these patients is relatively low, of the order of 2-6 per year for major hospitals. Also, patients are generally available for research for only a few hours/day at most. Patients vary considerably in cognitive capability, level of interest in participating, clinical status, and thus lots of variations have been observed in the performance of ECoG-based BCIs.

2.3 DATA COLLECTION

2.3.1 DATA ACQUISITION

Data were collected from six patients with medically intractable epilepsy who underwent phase 2 evaluation for epilepsy surgery with temporary placement of intracranial grid or strip electrode arrays and/or depth electrodes to localize seizure foci prior to surgical resection. All six patients were presented at Mayo Clinic Florida's multidisciplinary

surgical epilepsy conference, where the consensus clinical recommendation was for the participants to undergo invasive monitoring primarily to localize the epileptogenic zone. The study was approved by the institutional review boards by Mayo Clinic, University of North Florida, and Old Dominion University. All the participants gave their informed consent. Both s-EEG and i-EEG data were recorded using BCI2000, a general purpose BCI system [38]. Patients implanted with electrodes suffer from the implantation trauma and pain. It is difficult to simultaneously record s-EEG and i-EEG because of high chances of corruptive effects that can be caused because of the incision.

s-EEG data were recorded before the placement of the intracranial electrodes. They were recorded using an ElectroCap International cap with 32 electrodes distributed over the scalp based on the International 10-20 System [34]. All the s-EEG electrodes were referenced to the right mastoid and amplified.

Intracranial Electrode (AD-tech Medical Instrument Corporation, Wisconsin) placements and duration were based solely on the requirements of the clinical evaluation without any consideration for this study. All electrode placements were guided intra operatively by the Stealth MRI Neuronavigational system (Medtronic, Inc., Minnesota). Each participant had postoperative anterior-posterior and lateral radiographs to verify electrode locations. After electrode implantation, all participants were admitted to an ICU room with epilepsy monitoring capability. Clinical recordings were gathered using 32-or 64-channel amplifiers. The intracranial electrode locations are shown in Figure 7. All i-EEG electrodes were referenced to a scalp vertex electrode. Different subjects had different number of electrodes and at different locations as per their clinical requirements. Subject C had

only stereotactic depth electrodes in hippocampus. Subject A, B, and E had both an array grid and stereotactic depth electrodes to localize the epileptic seizures.

Both the s-EEG and i-EEG data were amplified and band pass filtered from 0.5 to 500 Hz. The data were digitized using two to four 16-channel g.USB amplifiers at a sampling rate of 1200 Hz. Such a high sampling rate was selected to be consistent with the i-EEG data recordings.

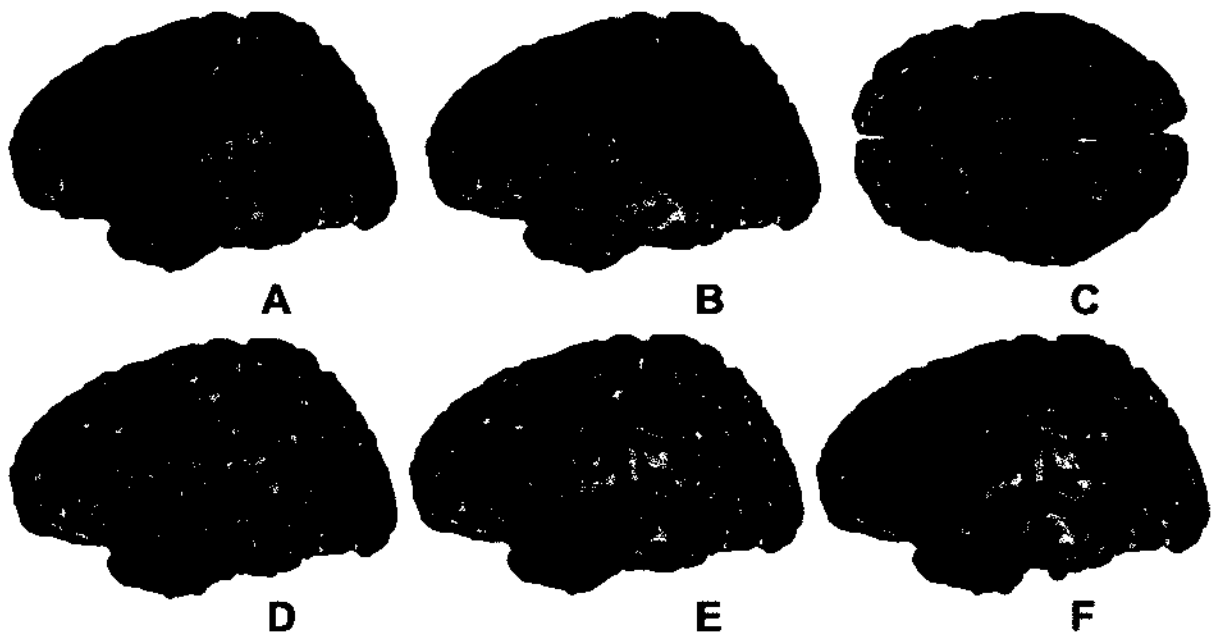


Fig. 7: Location of Intracranial electrodes (red ones show the electrodes that were used for recording). Different subjects had different numbers of electrodes and locations of i-EEG depending on the clinical requirement.

2.3.2 TASK, PROCEDURE AND DESIGN

The experimental protocol was based on the P300 speller and was consistent for both the s-EEG and i-EEG sessions. The patients sat in a comfortable chair (for s-EEG sessions) or hospital bed (for i-EEG sessions) approximately 75 cm from a video monitor. Each

session consisted of 8 – 11 experimental runs. Each run was composed of a word or series of characters. This set of characters was from a 6×6 matrix displayed on the monitor as shown in Figure 8 and was consistent for all the subjects. Each session consisted of between 32 – 39 character epochs. The rows and columns of the matrix were intensified for 100 ms with 75 ms between the intensifications [39]. A sequence of 15 row/column intensifications constituted one character epoch. Words were presented on the top left of the monitor, and the character currently specified for selection was listed in parentheses at the end of the letter string.

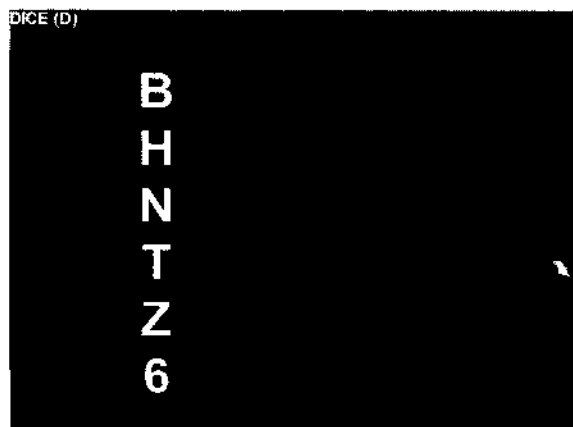


Fig. 8: The 6×6 matrix used in this dissertation. A row or column intensifies for 100 ms every 175 ms. The letter in the parentheses at the top of the window is the current target letter “D”. For this target, a P300 should be elicited when the fourth column or first row is intensified [39].

The subjects were asked to focus on a specified character of the matrix and count silently the number of times the target character was flashed. Classification was performed after each row and column had been intensified 15 times. Each session consisted of 36 character epochs. Each session of 36 characters corresponds to $36 \times 15 \times 12 = 6480$ stimuli (row/column intensifications). A single session lasted for approximately one hour.

2.3.3 DATA ANALYSIS

To assess the quality of the acquired s-EEG and i-EEG data, offline P300 speller accuracy was computed. For each subject and each session, an optimal linear classifier based on stepwise linear discriminant analysis (SWLDA) was trained. For each channel of the data, 800 ms (=192 samples) of the data segments were extracted following each flash for analysis. A feature vector corresponding to each stimulus was created by concatenating the extracted data segments by channel. Thus, for 6480 stimuli, 6480 feature vectors were generated. Each feature vector is of dimension, number of channels \times 192. A classifier was trained using these feature vectors.

SWLDA seeks optimal discriminant function by adding features to a linear equation in a stepwise fashion such that each feature contributes to the largest amount of unique variance. The algorithm performs a series of forward and backward regression procedures in discrete steps. Starting with no initial model terms, the single feature accounting for the most variance is added to the model. For any feature to be included into the model, it needs to be statistically significant, i.e. $p\text{-value} < 0.1$. In each step, the model evaluates every feature to determine the single feature that produces the highest $p\text{-value}$ and that feature is selected for inclusion.

After each entry, a backward stepwise regression is performed to remove any features that are no longer statistically significant, i.e. $p\text{-value} > 0.15$. This procedure is conducted because it is possible that a feature will no longer account for significant amount of unique variance after additional features have been included in the model. The process of addition and removal of feature variables is repeated until the pre-determined number of feature

variables have been selected for the model, or there are no more feature variables that satisfy the criteria of selection [15].

The P300 speller classification task can be considered as a binary classification problem defined as

$$w.x - b = 0 \quad (1)$$

where w corresponds to the feature weights generated by the classifier from the training data, x is the feature vector, and b is the bias for the model.

Since P300 is elicited when a target stimuli is presented, which corresponds to the intensification of a particular row and column, this classification of a character is equivalent to predicting the row and column. The predicted character corresponds to the intersection of the predicted row and column. Predicted row/column corresponds to the maximum of sum of scored features given by Equations (2) and (3).

$$Row_{predicted} = \max_{rows} \sum_{i_{row}} w.x_{i_{row}} \quad (2)$$

$$Column_{predicted} = \max_{columns} \sum_{j_{column}} w.x_{j_{column}} \quad (3)$$

In order to compute the classification accuracies for both s-EEG and i-EEG, the first 4 runs of the session were used to train the classifier and the remaining 4 runs of the session were used to test the classifier. Table I reports the s-EEG and i-EEG classification accuracies obtained after 15 flashes for all the subjects.

TABLE I: Classification accuracies for s-EEG and i-EEG for six subjects.

Subject	s-EEG (%)	i-EEG(%)
A	100	25
B	93	100
C	100	100
D	100	44
E	88	81
F	100	88

Table I shows that all the subjects attained greater than 80% classification accuracy for s-EEG, while 4 out of 6 subjects obtained greater than 80% accuracy for i-EEG. For each session, subjects typed 32 characters. Selection of each character corresponds to an independent event. The character selection is a Bernoulli trial with a probability of success equal to $\frac{1}{12}$. The selection of 32 characters follows a Binomial distribution. The mean of the Binomial distribution is given by np , where n is the number of characters and p is the probability of selection. Here $n = 32$ and $p = \frac{1}{12}$. Therefore, mean classification accuracy is 3%. Subjects A and D have low i-EEG accuracies compared to the corresponding s-EEG accuracies, and also compared to other subjects, but these accuracies are several standard deviations above the chance accuracy.

Since placement of i-EEG electrodes was solely based on the clinical requirements, this sub-optimal placement of the electrodes might have led to low i-EEG classification accuracies for particular subjects. Since i-EEG data were recorded after the surgery, the subjects also may have been experiencing pain, fatigue, medication effects, etc. that could adversely affect the i-EEG P300 performance. Regardless, the above-chance accuracies clearly indicate that the acquired data contains relevant P300 information for modeling.

CHAPTER 3

DIRECT MODEL

Electroencephalogram (EEG) recordings from the scalp and intracranial sites provide an indirect means to extract information about brain current sources. The electrodes used to record s-EEG are separated from the current sources in the brain by cerebrospinal fluid (CSF), the skull and the scalp. Due to the electrically low-conductive skull, the electric currents attenuate rapidly. Thus s-EEG is a spatially blurred representation of the cortical activity. This results in comparatively poor spatial resolution of s-EEG recording compared to i-EEG [30].

i-EEG is recorded from the surface of the brain. The surface of the brain is separated from the current sources by CSF and cerebral cortex. The absence of skull attenuation leads to superior spatial resolution of i-EEG as compared to s-EEG.

Since the skull and scalp tissue of the human head act as a volume conductor for the brain's electrical activity [29], the scalp recorded data can be considered as a linear mixture of the underlying intracranially recorded data [40]. This forms the basis of the first major contribution of this dissertation, which is the direct model. The direct model is designed to minimize the estimation error between the i-EEG and s-EEG ERP waveforms in a forward model.

3.1 MODELING SCALP ELECTROENCEPHALOGRAPH USING INTRACRANIAL ELECTROENCEPHALOGRAPH

The direct model is formed by using the i-EEG (intracranial) ERPs to model s-EEG (scalp) ERPs [40]. In this modeling approach, average target ERPs for both scalp and intracranial EEG were used to develop the model. Only target ERPs were considered for this model because these ERPs represent consistent and predictable evoked neural activity. Non-target stimulus data mainly consists of spurious background activity and thus were not considered for the model. Direct model represents each channel of s-EEG ERPs as a linear combination of the i-EEG ERPs.

3.1.1 METHODOLOGY

For extracting the ERPs from both the sessions (scalp and intracranial), certain pre-processing needs to be done. Most of the energy of low frequency ERPs like the P300 is concentrated below 20 Hz [39]. Also, 60 Hz power supply frequency and higher-frequency muscular artifacts should be eliminated. Thus, both s-EEG and i-EEG data were low pass filtered to 20 Hz to smooth the data. Further, data were decimated to 240 Hz to have a sufficient number of samples for the purpose of modeling and ERP visualization.

ERPs are assumed to be consistent and time invariant for both s-EEG and i-EEG, which is supported by the respective classification performances. Target stimulus ERPs correspond to the ERPs that are generated from a flash that the subject was instructed to focus on. For both s-EEG and i-EEG data, 800 ms of data following each intensification were extracted as Target ERP. All the s-EEG target ERPs for all the runs (960 ERPs) were averaged across all the trials to form the *Archetype s-ERP*. For i-EEG, only the first half of

the target ERPs (480 ERPs) were averaged to form the *Training i-ERP* and the remaining second half were averaged to form the *Testing i-ERP*. *Training i-ERPs* were used in an ordinary least square linear regression model to model each *Archetype s-ERP* as shown in Figure 9.

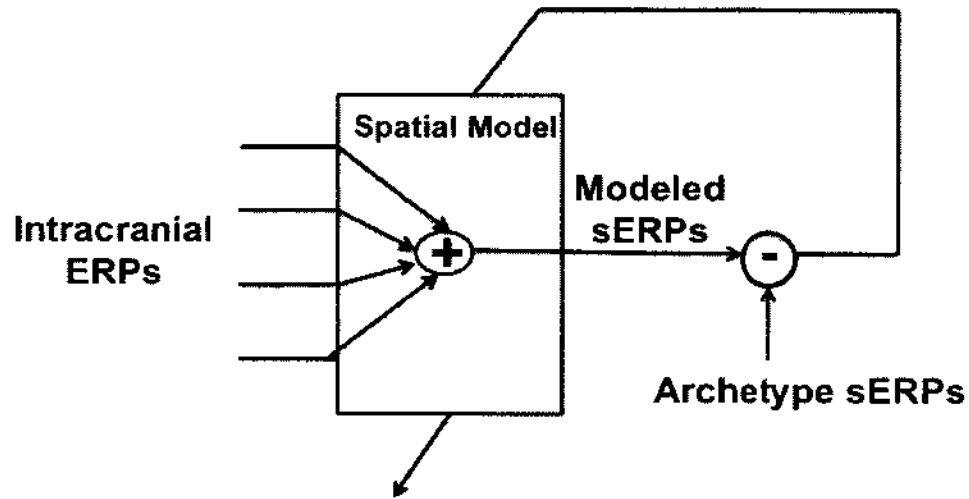


Fig. 9: Direct ERP Modeling Block Diagram. A linear combination of i-ERPs are used to model each s-ERP independently using ordinary least square regression.

$$s-ERP_{Archetype} = b \times iERP_{Training} + c \quad (4)$$

where b is the weight matrix generated by the regression model and c is a constant. Testing i-ERPs were used to validate the model, and the corresponding *Modeled s-ERPs* were generated.

$$s-ERP_{Modeled} = b \times iERP_{Testing} \quad (5)$$

3.1.2 RESULTS

In order to validate the Direct model, Root Mean Square Error (RMSE) was computed between the Archetype and Modeled s-ERPs. Each Archetype s-ERP was scaled to have unity variance. The same scale factor was applied to the respective Modeled s-ERPs. This scaling removes the amplitude dependencies when comparing RMSE across channels. Figure 10 shows the RMSE plots for the developed model.

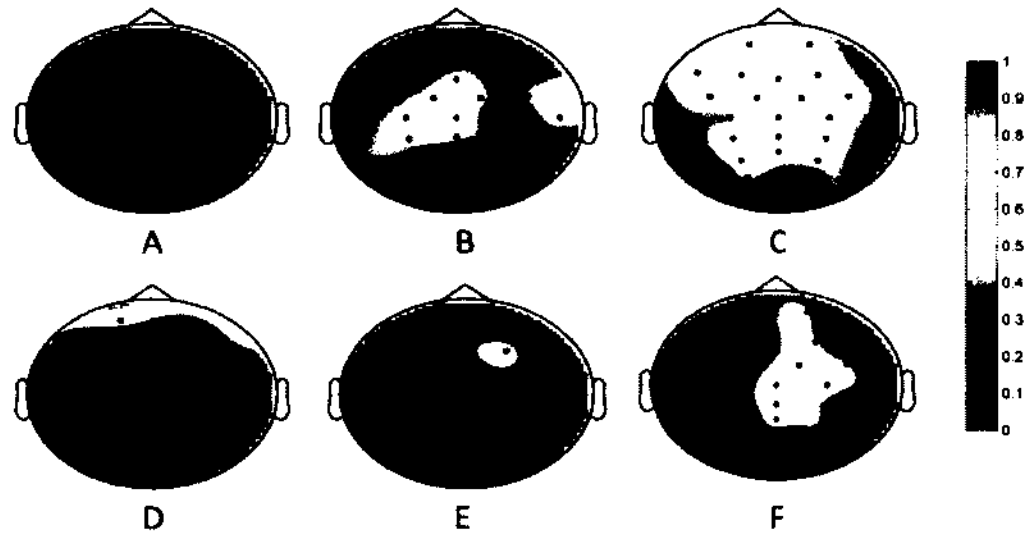


Fig. 10: Root Mean Square Error obtained between archetype ERPs and modeled ERPs using the direct modeling approach.

Figure 10 shows that RMSE is quite high for most of the channels for all the six subjects. One possible reason for the high RMSE could be the noisy i-EEG ERPs from certain channels that do not contain useful P300 information. In order to improve the model, a channel selection procedure was employed. This approach was based on considering only those channels of iEEG that have useful P300 information.

3.2 DIRECT MODEL WITH CHANNEL SELECTION

To assess the quality of each channel of the recorded data, single channel accuracies (SCA) were computed for both s-EEG and i-EEG. SCA were computed by considering the features from a single channel. For each channel, an optimal linear classifier was trained using first the four runs of the session and tested on the remaining four runs of the session. The SCA gives an indication of the relative importance of each channel for discriminating the ERPs, or in other words, how much is each channel's contribution towards P300 classification. Figures 11 and 12 show the single channel accuracies obtained for s-EEG and i-EEG for all six subjects, respectively.

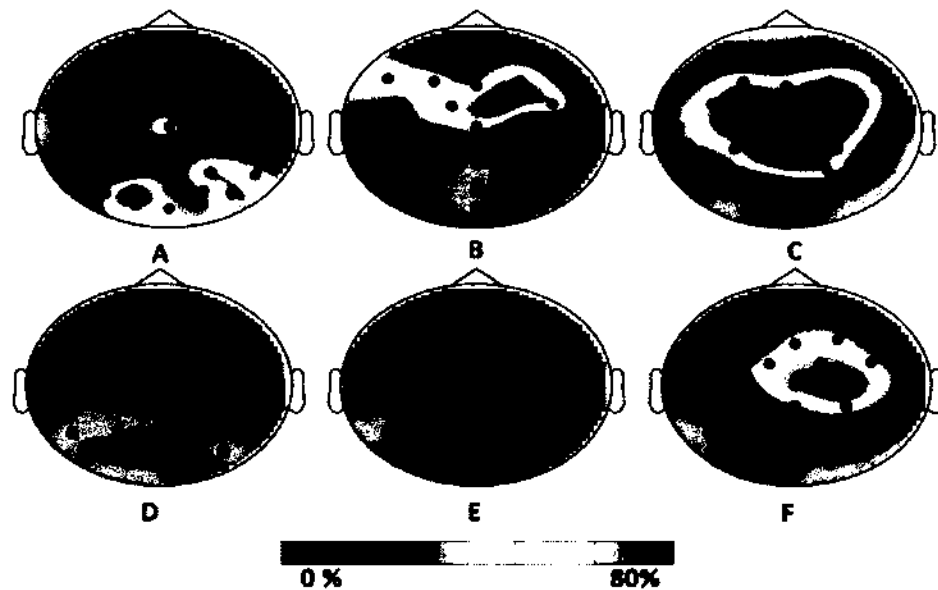


Fig. 11: s-EEG single channel accuracies (SCA) topographies for the six subjects (A-F). Black dots represent the fixed 32-channel electrode positions according to the International 10-20 system [34]. SCA was determined using the ERP amplitude features from a single channel to derive the respective channel's classifier based on [39].

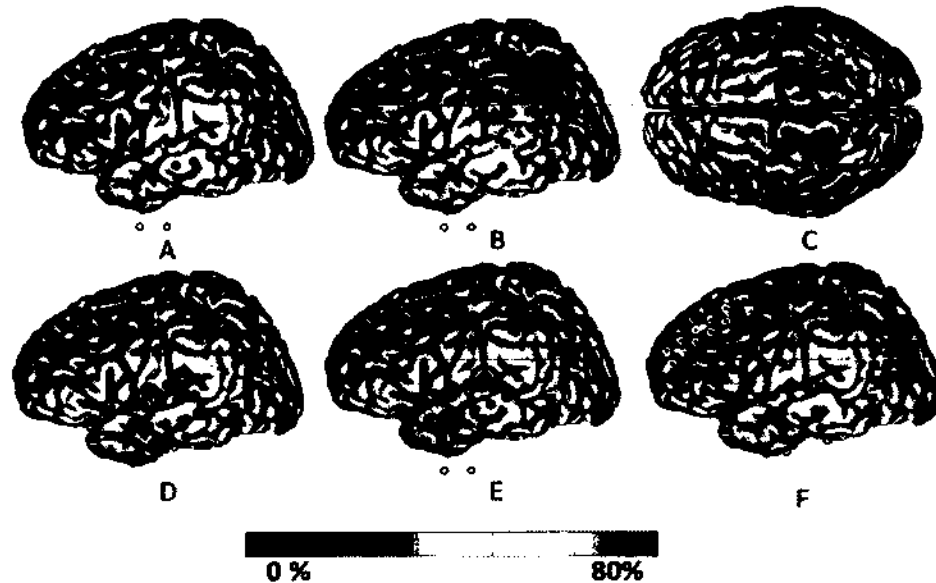


Fig. 12: iEEG single channel accuracies (SCA) topographies for the six subjects (A-F). For each subject, iEEG SCA topographies are plotted on generic brain models with electrode locations indicated by the circles. The black circles represent the electrodes that were used for the BCI recordings and modeling, whereas white electrodes were only used for clinical recordings and not represented in the models.

As can be seen from Figures 11 and 12, some of the channels of s-EEG and i-EEG have zero SCA classification accuracy. Thus, these channels mainly consist of background noise and do not contribute any information for discriminating ERPs. Thus, Direct models were constructed by considering only those i-EEG channels that are above a certain threshold. For different subjects, the optimal threshold for channel selection was empirically selected. This threshold varied from 6 – 19%. The individual thresholds were selected on the basis of modeling accuracy. Since there was lot of variability in the SCA across different subjects, different thresholds were selected. All the i-EEG channels with SCA below the threshold were excluded from the model, but all of the s-EEG channels were retained for a complete evaluation and visualization of the forward modeling.

Figure 13 shows the schematic representation of the direct model with channel selection. A model was developed from the s-EEG and selected i-EEG ERPs using least square linear regression as discussed in Section 3.1.1.

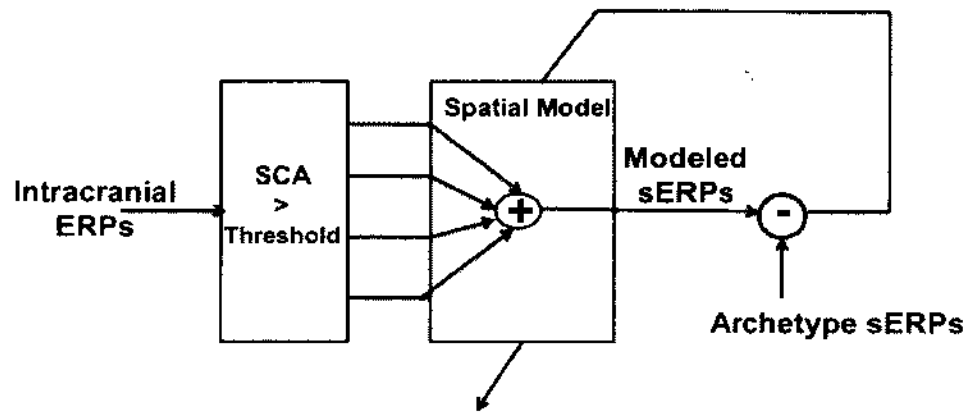


Fig. 13: Direct modeling block diagram with optimally selected iEEG channels. A linear combination of the optimally selected iERPs are used to model each s-ERP independently using ordinary least squares regression.

3.2.1 RESULTS

The channel selection on the basis of SCA significantly improved the performance of the model. Selected ERPs and spatial filters from the Direct model are shown in Figure 14. The first column corresponds to the three i-EEG ERPs for each subject, corresponding to the channels with highest SCA. The second column shows the RMSE topographies for all the six subjects. The RMSE was scaled as explained in Section 3.1.2. The third and fourth columns show the Modeled and Archetype s-ERPs and the corresponding spatial models respectively for the channel with lowest RMSE. The fifth and sixth columns correspond to Modeled and Archetype s-ERPS and the spatial model for channel Cz. The channel Cz

was considered because this channel is considered as the most important location of the P300 response.

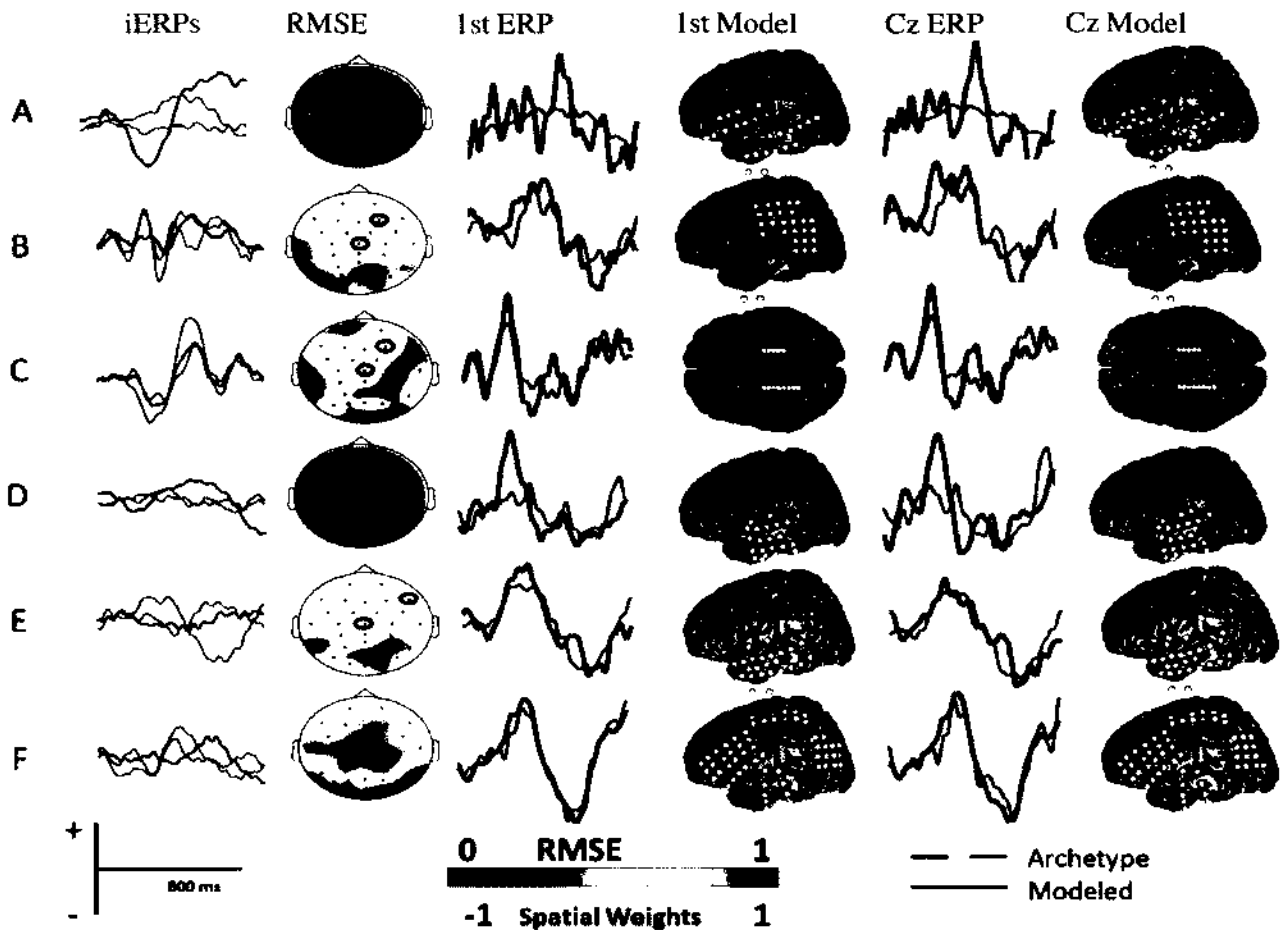


Fig. 14: ERPs and Spatial models for Direct model. The first column shows the three iERPs for each subject (A-F) corresponding to channels with the highest SCA, with red representing the highest SCA and blue representing the second highest SCA. The second column shows the RMSE topographies, with the channel corresponding to the lowest RMSE circled in purple and channel Cz circled in green. The third and fourth columns show the modeled ERPs and the corresponding spatial models, respectively, for the channel with the lowest RMSE. The fifth and sixth columns show the modeled ERPs and the corresponding spatial models for channel Cz. The channel weights for the spatial models were normalized to have a maximum magnitude of 1.

To evaluate the performance of the developed model in a practical sense, classification performance was evaluated using optimal s-EEG derived classifier for each subject. Modeled s-EEG was generated by using the spatial model. All the data (Archetype s-EEG and Modeled s-EEG) were low pass filtered and decimated to 20 Hz. For each channel, 800 ms of data were extracted following each flash. An optimal linear classifier for each subject based on stepwise linear discriminant analysis (SWLDA) was trained using the Archetype s-EEG (both target and non-target). The second half of modeled s-EEG ERPs (both target and non target) generated by the spatial model was used to test the classifier. The score was obtained from the classifier, which can be represented as the percentage of correctly classified characters [39].

Table II gives the classification accuracies obtained for the modeling approach. The classification accuracies obtained using the optimal linear classifier derived from s-EEG and iEEG are also reported for comparison.

TABLE II: Classification Accuracies for Direct model with channel selection. Columns two and three correspond to the optimal linear classifier derived from the s-EEG and iEEG data. The fourth column gives the classification accuracies from Direct model with channel selection.

Subject	s-EEG (%)	iEEG(%)	Direct Model (with channel selection)(%)
A	100	25	19
B	93	100	38
C	100	100	50
D	100	44	19
E	88	81	63
F	100	88	32

3.2.2 DISCUSSION

The Direct model shows that s-ERPs can be accurately modeled as a linear combination of the underlying i-ERPs. Spatial filter weights given in Figure 14 indicate that relatively few i-EEG channels contribute to the modeled s-EEG ERPs. These weights also tend to occur in small spatially localized groups or in more distant bipolar pairs. The classification accuracies reported in Table II for all the subjects are not suitable for practical performance, but are several standard deviations above the chance accuracy (3%). This poor classification performance can be explained in part by the fact the Direct model gives equal emphasis to all the time points of the data, some of which are not important for classification.

CHAPTER 4

DIRECT MODELS WITH SPATIAL FILTERING

The Direct Model was designed by considering the ERP waveforms from both the scalp and intracranial ERPs. The Modeled s-ERPs generated from the direct model matched very well with the Archetype s-ERPs. However, this model did not result in acceptable BCI performance. This chapter explores potential enhancements to the direct modeling using pre-processing via spatial filters.

Since the skull has low conductivity and the human head acts as a volume conductor, the s-EEG is essentially spatially lowpass filtered (i.e., a spatially blurred representation of the underlying cortical activity). This smearing effect leads to highly correlated s-EEG. Various spatial filtering techniques can be applied to the s-EEG to enhance sensitivity, improve source localization, and suppress artifacts. s-EEG data have low signal-to-noise ratio (SNR), and spatial filtering techniques help in improving the SNR of the recorded signals.

Spatial filtering techniques can be classified as data dependent or data independent. Data-independent spatial filtering techniques use fixed-geometry relationships to determine the spatial filter weights [32]. Common data independent spatial filters for EEG include the common average reference (CAR) spatial filter and the surface laplacian. The CAR is implemented by first computing the global mean of all the channels and then subtracting the computed mean from each individual channel. This spatial filtering technique

removes the common artifacts and noise present across all the channels. The surface Laplacian eliminates the correlated activity of the spatially adjacent channels by subtracting the mean of all the channels at a fixed radial distance from the central channel of interest [32].

Data-dependent spatial filtering techniques are derived from the recorded data. In this dissertation, three different data dependent spatial filtering techniques, namely, principal component analysis (PCA), independent component analysis (ICA) and stationary subspace analysis (SSA) were applied on s-EEG. The corresponding direct models were generated in order to evaluate the efficacy of preprocessing the signals with these common signal subspace decomposition methods.

4.1 DIRECT MODEL WITH PRINCIPAL COMPONENT ANALYSIS

Principal component analysis (PCA) is a non-parametric method of extracting relevant information from the data. It simplifies the description of the data set by computing the most meaningful basis to re-express the noisy data [41]. PCA finds a linear transformation of the data that maximizes the variance of the transformed data. PCA is computed by finding the eigenvectors of the covariance matrix as given in Equation 6.

$$X^T X \alpha = \lambda \alpha \quad (6)$$

where X represents the s-EEG with N channels, $X^T X$ corresponds to the covariance matrix, α is an eigenvector with a corresponding eigenvalue λ . The set of all eigenvectors constitutes the new orthogonal basis, named spatial weight W , on which scalp data are projected. The basis obtained is a linear combination of the N channels. The eigenvector

with the highest eigenvalue corresponds to the most significant principal component of the dataset. All the eigenvectors are arranged from highest to lowest, corresponding to the significance of the principal components. The transformed data set is obtained by projecting the original data onto the new orthogonal basis

$$Y = WX \quad (7)$$

where W in Equation 7 is the spatial weight that transforms the recorded s-EEG. Each row of the spatial weight W corresponds to a particular spatial filter. Each row of Y is the weighted sum of all the channels of X , and weights for each channel are defined by the corresponding rows in W [41].

4.1.1 METHODOLOGY

The Direct model with PCA was developed by applying the PCA on the s-EEG. For i-EEG, only the channels with SCA (single channel accuracy) above a certain threshold were considered, as discussed in Chapter 3 Section 3.2. PCA was applied only on the s-EEG to extract the relevant features and thus improve the SNR. The principal components corresponding to 98% variance were selected for modeling. This threshold value of variance for principal components was selected so that we have significant number of components for the modeling. The 98% variance corresponded to optimum modeling accuracy.

Direct model with PCA was developed following the similar methodology as described in previous chapter in Section 3.1.1. Figure 15 shows the schematic representation of the Direct model with spatial filter, here spatial filter corresponds to PCA.

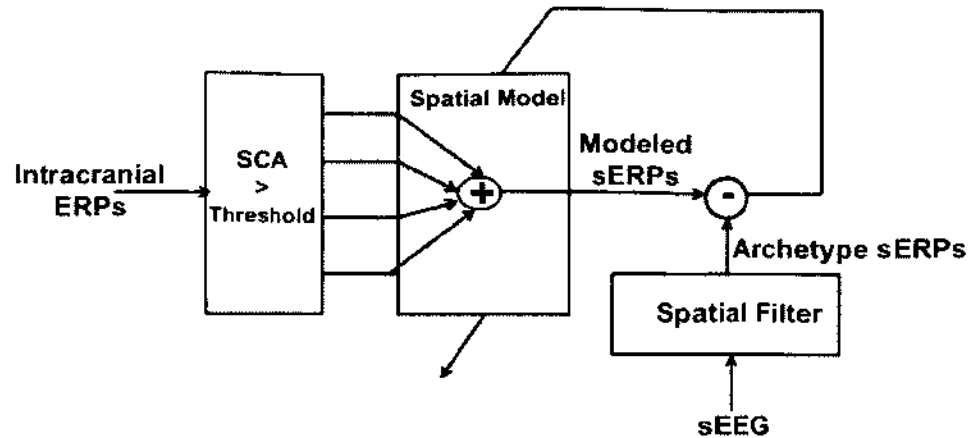


Fig. 15: Schematic Diagram showing the Direct ERP based Model with Spatial Filter

4.1.2 RESULTS

To evaluate the performance of the developed model, Root Mean Square Error (RMSE) was computed between each Archetype s-ERP channel and Modeled s-ERP. To compute the RMSE for all the scalp channels, inverse PCA was applied on both Archetype s-ERP and Modeled s-ERP for each subject. RMSE was scaled following the similar procedure as described in section 3.1.2. Column 1 of Figure 16 shows the RMSE between Archetype s-ERP and Modeled s-ERP for all the channels. Columns 2 and 3 correspond to the Archetype s-ERP and Modeled s-ERP waveform and corresponding spatial weights for the channel with minimum RMSE. Columns 4 and 5 show the waveforms and spatial weights for channel Cz.

From Figure 16, it can be seen that RMSE for most of the subjects and channels is quite high. Only for Subject F, RMSE for the central and parietal channels is quite low. The Archetype and Modeled s-ERPs for 1st channel (i.e. channel with minimum RMSE) and channel Cz, are nicely following each other for four of the six subjects. These waveforms

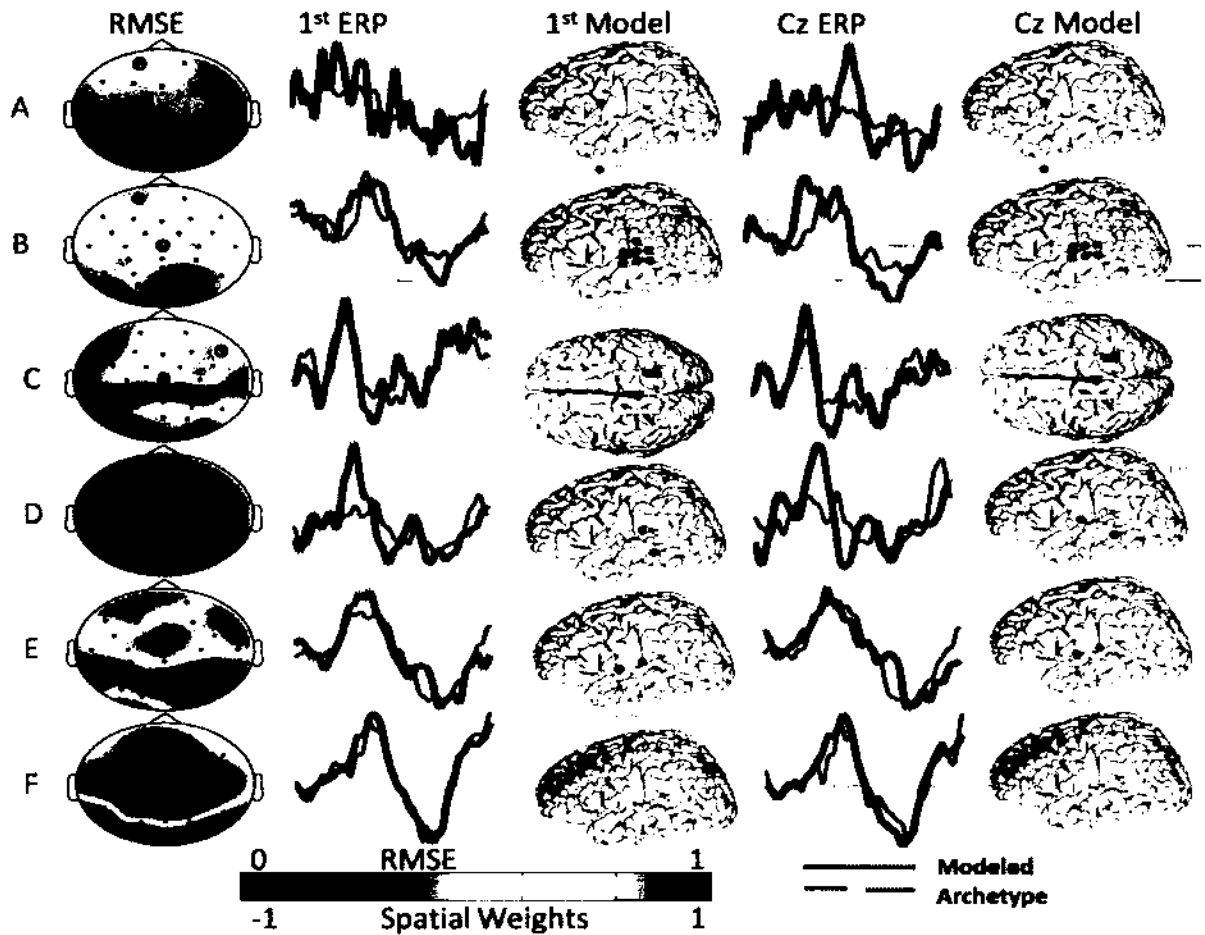


Fig. 16: ERPs and Spatial models for Direct model with PCA. The first column shows the RMSE topographies for all the subjects with the lowest RMSE channel (i.e. 1st channel) circled in purple and channel Cz circled in green. The second and third columns show the Modeled and Archetype s-ERPs and the corresponding spatial models for the 1st channel. The fourth and fifth columns show the Modeled and Archetype s-ERPs and the spatial models for channel Cz. The channel weights for the spatial models were normalized to have a maximum magnitude of 1.

indicate that the Direct model using PCA works well in predicting the s-ERPs from the i-ERPs. As can be seen from columns 4 and 6 of Figure 16, only a few intracranial channels contribute in modeling the scalp EEG ERPs.

4.2 DIRECT MODEL WITH INDEPENDENT COMPONENT ANALYSIS

Independent Component Analysis (ICA) is a technique that decomposes the data into statistically independent components. PCA uses second order statistic of data, i.e. covariance to find the uncorrelated components. ICA uses higher order statistics to find statistically independent components. ICA is defined as an optimization problem to minimize mutual information between the source components using higher order statistics to measure non-Gaussianity [42].

The central limit theorem states that sum of a large number of independent processes tends toward a Gaussian distribution. Therefore, if Y is assumed to be a set of truly independent channels, X must follow a Gaussian distribution. ICA computes the spatial weight matrix W such that it maximizes the non-Gaussianity of Y . There are many algorithms that use different metrics like minimization of mutual information or maximum likelihood estimation to compute statistically independent components.

For this dissertation, the FastICA algorithm [43] was used to extract the independent components from the dataset. The FastICA algorithm finds a direction for each channel such that $w^T x$ maximizes the non-Gaussianity. This algorithm uses negentropy to measure non-Gaussianity. Negentropy is defined as

$$J(X) = H(X_{gauss}) - H(X) \quad (8)$$

where X_{gauss} is a Gaussian random variable of the same covariance matrix as X , $H(X)$ is the differential entropy of the random variable X defined as

$$H(X) = - \int f(X) \log(f(X)) dX \quad (9)$$

where $f(X)$ is the density function. Negentropy is always a negative number. $J(X)$ is equal to zero iff X has a Gaussian distribution.

It is computationally difficult to estimate density and thus negentropy. But negentropy can be approximated as

$$J(X) \propto [E[G(Y)] - E[G(v)]]^2 \quad (10)$$

where G is a non-quadratic function and v is assumed to be zero mean and unit variance. G must be selected wisely, such that approximation of negentropy is a good estimate.

The FastICA algorithm is based on a fixed point iteration scheme. The step by step procedure followed to find each random vector w , such that the resultant components of Y are independent, is as follows:

1. Choose an initial (random) weight vector w .
2. Let

$$w^+ = E[xg(w^T x)] - E[g'(w^T x)]w$$

3. Let

$$w = \frac{w^+}{\|w^+\|}$$

4. These steps are repeated until old and new values of w point in the same direction, i.e. $w_{old}w_{new} = 1$.

The FastICA algorithm computes independent components one by one. After p components have been estimated, w_{p+1} is estimated. After each iteration, projection of w_{p+1}^T is subtracted from the previously estimated p -vector, then w_{p+1} is normalized.

$$w_{p+1} = w_{p+1} - \sum_{j=1}^p w_{p+1}^T w_j w_j$$

This process decorrelates the output after every iteration and thus prevents different vectors from convergence to the same maxima. FastICA algorithm can estimate both super and sub Gaussian independent components.

4.2.1 METHODOLOGY

Direct model with ICA was developed by applying ICA on the s-EEG. For i-EEG, only the channels with single channel accuracy (SCA) above the optimally selected threshold were considered. For both s-EEG and i-EEG same preprocessing steps were applied as described in Section 3.1.1. Before performing ICA on the s-EEG, PCA was applied to extract the uncorrelated components. On the uncorrelated channels, FastICA algorithm was applied to extract the independent components. All the independent components generated did not have relevant information corresponding to the task. Kurtosis was used as a criterion to select the relevant independent components. Kurtosis is defined as

$$kurt(y) = E[y] - 3[E[y^2]]^2 \quad (11)$$

Kurtosis is a measure of non-Gaussianity. If a random variable is Gaussian, then kurtosis is equal to zero. If kurtosis has a non zero value, then random variable can be either super Gaussian or sub Gaussian. Positive value of kurtosis, corresponds to a super Gaussian distribution. A super-Gaussian distribution indicates that much of the variation in the signal is caused by the infrequently occurring large deviation or a tailed distribution. This kind of distribution is common in independent signals. Thus, independent components with positive kurtosis value were selected for developing the model. The set of selected independent components were used to transform the s-EEG [43]. Figure 15 shows the schematic representation of the Direct model with spatial filter, where spatial filter for this model corresponds to ICA.

A least square linear regression model was developed using Archetype s-ERP to generate Modeled s-ERP using the selected independent components of s-EEG and i-EEG. Same procedure was followed to develop the model as described in Section 3.1.1.

4.2.2 RESULTS

Root Mean Square Error (RMSE) was used as a metric to evaluate the performance of the model. The Archetype and Modeled ERPs were projected back to the scalp by multiplying with inverse ICA and PCA spatial matrices. RMSE was computed between the transformed Archetype and Modeled s-ERP's.

Column 1 of Figure 17 shows the RMSE between the Archetype s-ERP and Modeled s-ERP. RMSE for most of the subjects and most of the channels was quite high. Only for Subject E, the RMSE between the Archetype and Modeled s-ERP for all the channels was low, indicating that most of the channels were modeled accurately. In order to see the

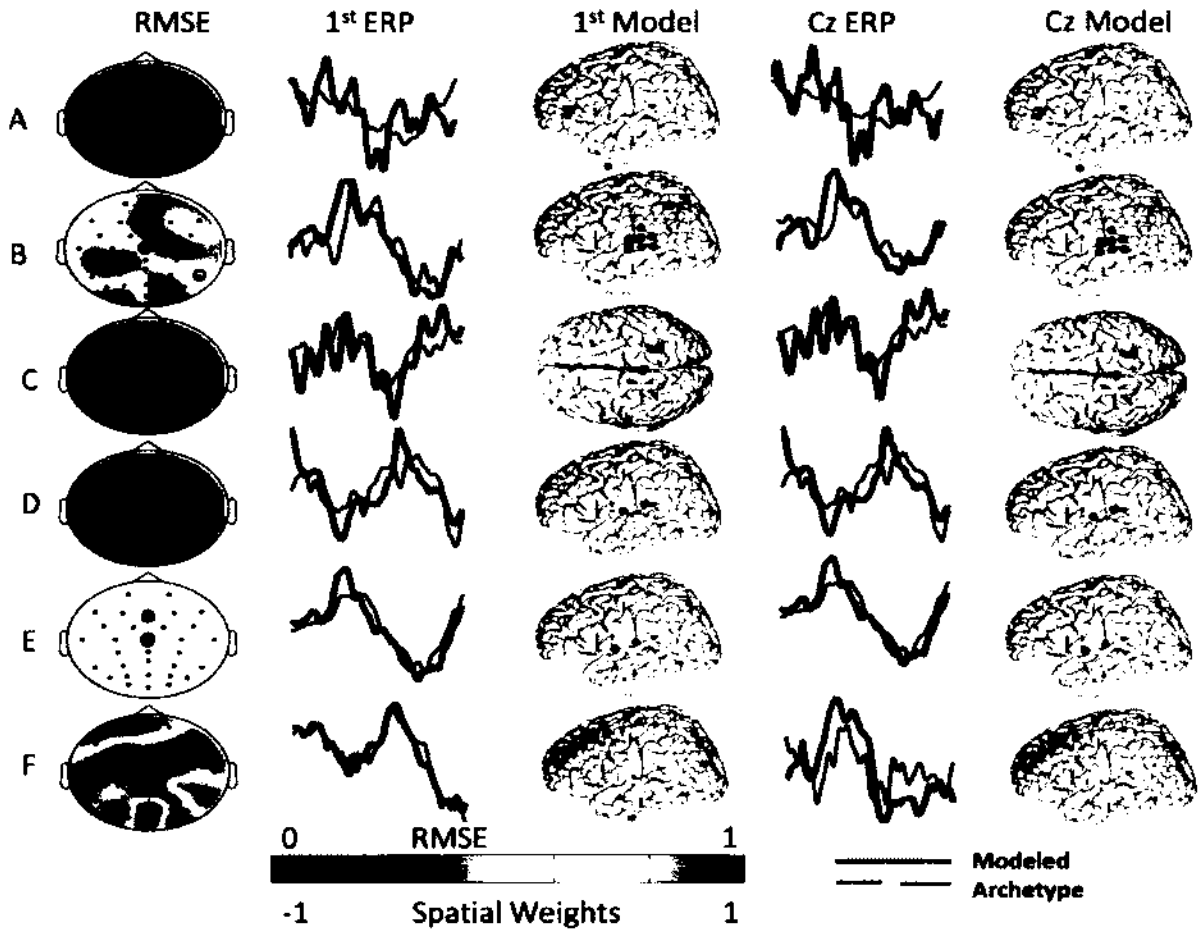


Fig. 17: ERPs and Spatial models for Direct model with ICA. The first column shows the RMSE topographies with the channel corresponding to the lowest RMSE circled in purple, termed as 1st channels and channel Cz circled in green. The second and third columns show the Modeled and Archetype s-ERPs and the spatial models for the 1st channel. The fourth and fifth columns show the Modeled and Archetype s-ERPs and the spatial models for channel Cz. The channel weights for the spatial models were normalized to have a maximum magnitude of 1.

performance of the model in terms of the Modeled ERPs, Archetype and Modeled s-ERP waveforms for the 1st channel, (the channel with least RMSE), are plotted in Column 2 of Figure 17. Column 3 shows the corresponding spatial weights for the 1st channel for all the subjects. Figure 17 also displays the Archetype and Modeled s-ERPs and the respective spatial weights for channel Cz. As can be observed from the spatial weights in Figure 17, very few i-EEG channels contribute towards the Modeled s-ERPs. The Modeled s-ERP for most of the subjects were following the Archetype s-ERP, thus validating the performance of the developed model.

The Direct model with ICA could accurately predict the s-ERP from the iERP as shown in Columns 2 and 4 of Figure 17.

4.3 DIRECT MODEL WITH STATIONARY SUBSPACE ANALYSIS

In the previous two sections, linear models were developed by applying spatial filtering techniques PCA and ICA. Both these techniques assume the data to be stationary. Both scalp and intracranial EEG are non-stationary in nature. Also, PCA and ICA spatial filtering techniques did not take the P300 speller task information into consideration for extracting the relevant components.

Both scalp and intracranial EEG signals come from multiple neural sources inside the brain. Any non-stationary source can make all the channels non-stationary. Stationary Subspace Analysis (SSA) is a technique which separates the stationary components of the data from the non-stationary components. Since target ERPs are assumed to be stationary signals in the presence of non-stationary background activity, only target scalp and intracranial signals were used for SSA. The stationary components from both scalp and

intracranial EEG was extracted by applying SSA. Stationary components of both signals were used to develop a new linear model relating scalp and intracranial ERPs.

SSA assumes that the multivariate time series, $X(t)$, is generated as a mixture of some stationary and non-stationary sources [44], as given by Equation 12.

$$X(t) = WS(t) \quad (12)$$

Assuming that there are d number of stationary sources, $D - d$ number of non-stationary sources, D being the number of sources/channels in the dataset, $X(t)$ can be written as given by Equation 13.

$$X(t) = [W^s \ W^n][S^s(t) \ S^n(t)] \quad (13)$$

where $S^s(t)$ refers to d stationary source signals or **s-sources**, $S^n(t)$ refers to $D - d$ non-stationary source signals or **n-sources**, W^s spans the subspace of s-sources and W^n spans the subspace of n-sources. SSA estimates a linear transformation from $X(t)$ that separates the s-sources from the n-sources.

Let the estimated *Mixing matrix* be given by \hat{A}

$$\hat{A} = [\hat{A}^s \ \hat{A}^n] \quad (14)$$

Let the estimated *Demixing matrix* be given by \hat{W}

$$\hat{W} = \hat{A}^{-1} = [\hat{W}^s \ \hat{W}^n]^T \quad (15)$$

where \hat{W}^s projects the observed data into the estimated s-subspace and \hat{W}^n projects the observed data into the estimated n-subspace.

$$A^s = \hat{A}^s M_1 + \hat{A}^n M_2$$

$$A^n = \hat{A}^s M_3 + \hat{A}^n M_4$$

The estimated s-source and n-source can be expressed as

$$\hat{s}^s = M_1 s^s + M_3 s^n \quad (16)$$

$$\hat{s}^n = M_2 s^s + M_4 s^n \quad (17)$$

Since s-source should have only s-sources, M_3 can be approximated to zero. Thus, the estimated s-source and n-source can be expressed as

$$\hat{s}^s = M_1 s^s \quad (18)$$

$$\hat{s}^n = M_2 s^s + M_4 s^n \quad (19)$$

The estimated s-source is a linear combination of the true s-sources and n-sources. To estimate the stationary sources, SSA minimizes pairwise distance between the distributions of the projected data using Kullback-Leibler (KL) divergence. Only the first two moments are computed to confirm the stationarity of the sources. The demixing matrix (\hat{W}) is given by solving the following optimization problem

$$\hat{W} = \underset{BB^T=I}{\operatorname{argmin}} \sum_{i < j} KL[N(I^d, B\hat{\mu}_i, I^d B\hat{\Sigma}_i(I^d B)^T)N(I^d B\hat{\mu}_j, I^d B\hat{\Sigma}_j(I^d B)^T)] \quad (20)$$

where $\hat{\mu}_i$ is the estimated mean for the dataset X_i and $\hat{\Sigma}_i$ is the corresponding covariance matrix. The conjugate gradient procedure is used to solve the optimization problem.

4.3.1 METHODOLOGY

The Direct model with SSA was developed by extracting the target ERPs for both s-EEG and i-EEG. The number of stationary components for both the data sets were empirically determined for all the subjects. The direct model using least square linear regression was developed by following the same procedure as given in Section 3.1.1. Only the extracted stationary components of both s-ERP and i-ERP were used for the model. Figure 18 shows the schematic representation of the Direct model with SSA.

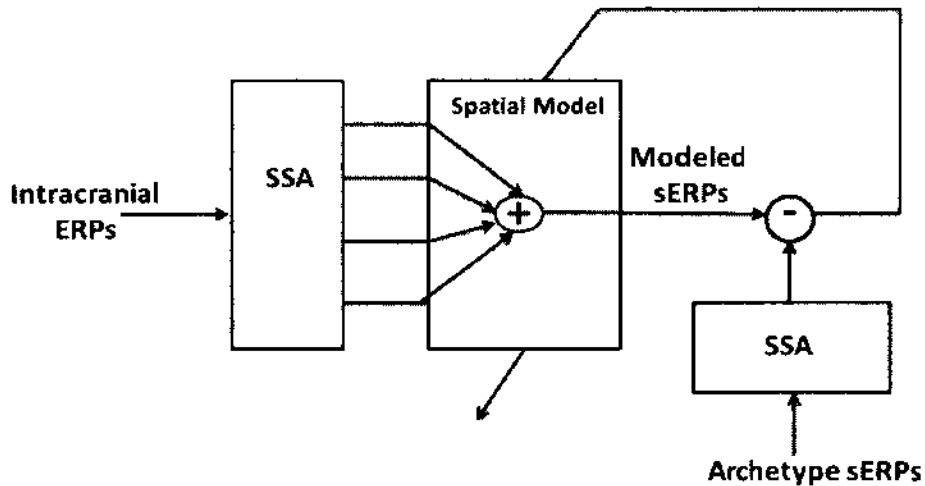


Fig. 18: Schematic Diagram showing the Direct model with Stationary Subspace Analysis

4.3.2 RESULTS

RMSE between the Archetype and Modeled s-ERPs was evaluated to validate the performance of the Direct model with SSA. The Archetype and Modeled s-ERPs were projected back to the scalp by multiplying both the ERPs with the mixing matrix as given in Equation 14.

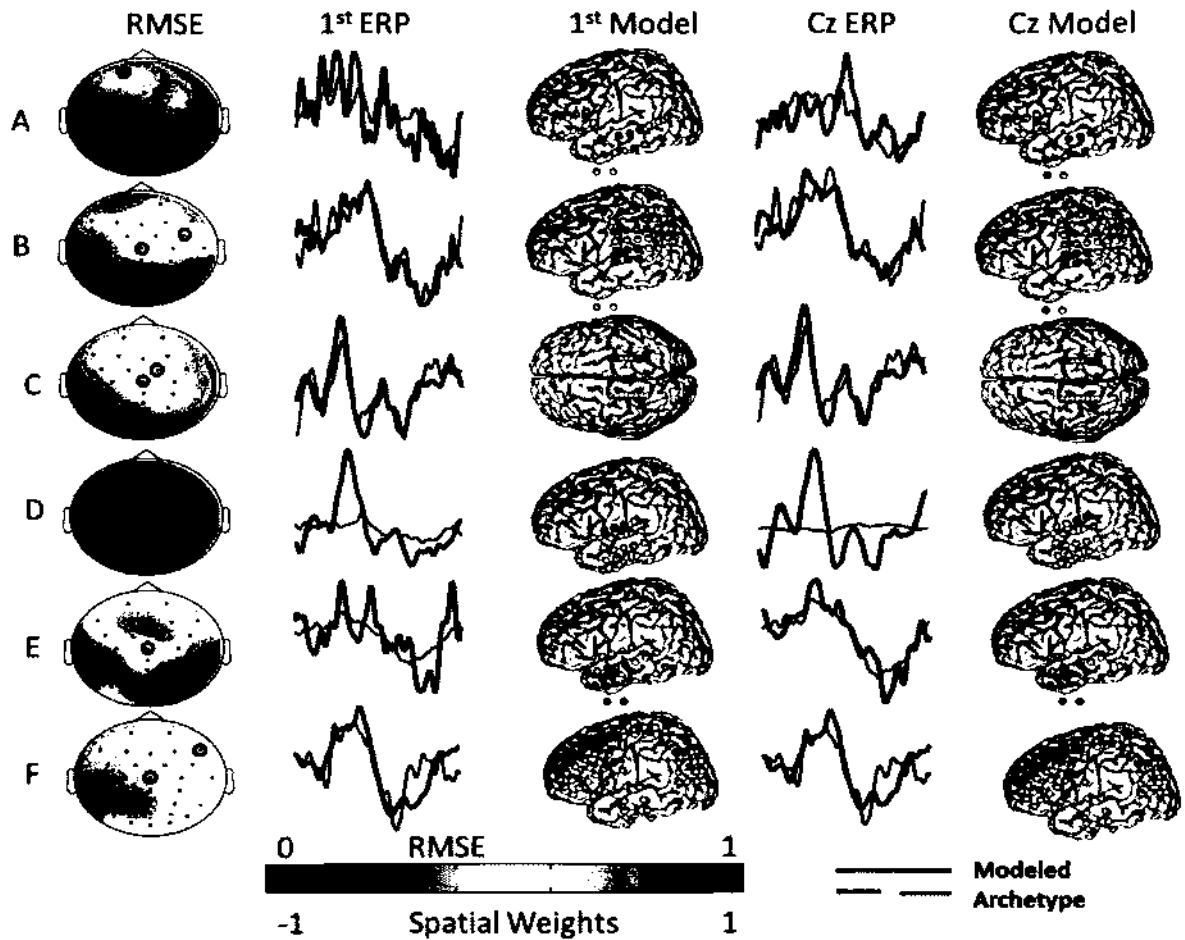


Fig. 19: ERPs and RMSE for Direct model with SSA. The first column shows the RMSE topographies with the channel corresponding to the lowest RMSE (1st channel) circled in purple and channel Cz circled in green. The second and third columns show the Modeled and Archetype ERPs and spatial weights for the first channel. The fourth and fifth columns show the Modeled and Archetype ERPs and spatial weights for the Cz channel.

Column 1 of Figure 19 shows the RMSE between the Archetype and Modeled s-ERPs for all six subjects. Second and fourth columns of Figure 19 show the Archetype and Modeled s-ERPs for the first channel (channel with minimum RMSE) and Cz channel, respectively. As can be seen from the plotted ERPs, for most of the subjects, the Modeled and Archetype s-ERPs are in accordance with each other. The third and fifth columns of Figure 19 correspond to the spatial weights obtained for the first and Cz channel respectively. These spatial weights indicate that all the channels contribute to the s-ERPs.

4.4 COMPARISON

Three different spatial filtering techniques (PCA, ICA and SSA) were applied to improve the direct model relation scalp and intracranial EEG. RMSE for all the models was computed to evaluate the model's performance. All the three models had similar performance. To further evaluate the performance of the developed direct models with spatial filters, the classification performance was computed. The s-EEG and i-EEG (target and non target) were multiplied with the corresponding spatial filters. Using these transformed s-EEG and i-EEG datasets, similar procedure as outlined in Section III.2.2 was followed to train and test the classifier for each subject.

Table III gives the classification accuracies obtained for all the models, Direct model (with channel selection), Direct model with PCA, Direct model with ICA, and Direct model with SSA. As can be seen from Table III that the classification accuracies for all the subjects for all the models are above chance, but do not correspond to acceptable BCI performance. Both PCA and ICA computation do not consider P300 speller task infor-

TABLE III: Classification accuracies for Direct models. Columns two and three correspond to optimal linear classifier derived from the s-EEG and iEEG data. The fourth column gives the results from Direct model with channel selection. The fifth, sixth and seventh columns give the classification accuracies from Direct model using PCA, ICA, and SSA, respectively.

Subject	s-EEG (%)	i-EEG(%)	Direct (%)	PCA (%)	ICA (%)	SSA (%)
A	100	25	19	25	25	25
B	93	100	38	56	50	50
C	100	100	50	44	38	56
D	100	44	19	13	13	38
E	88	81	63	56	69	69
F	100	88	32	31	19	38

mation and the relevant component extracted from the s-EEG may not be correlated with the task. A comparatively low power channel that is highly correlated with the task may not be included in the selected components. ICA is based on the assumption that the data can be decomposed to independent components, which may not be true, particularly if the assumed number of independent components is not accurately determined. SSA extracts the stationary components from the scalp and intracranial ERPs, assuming that only target ERPs contain the stationary information.

Classification accuracies were computed using both the target and non-target ERPs from both the datasets (scalp and intracranial). Both target and non-target s-EEG and i-EEG were transformed to the new domain by using the spatial filter generated for only target ERPs. Since spatial filters were computed using only target ERPs, this could lead to poor BCI performance.

The classification accuracies obtained for all the direct models are comparable. The classification accuracies obtained from the direct model with SSA are highest for all the

subjects as compared to other models, although this difference is not significant.

In summary, all the models could accurately estimate the Archetype s-ERPs with negligible subject-specific differences. The developed models also achieved above chance classification accuracies but not acceptable BCI performance. This again can be attributed to the fact that the direct models were developed by considering the waveforms and not the BCI performance. Thus, this motivates the need for a model that considers BCI Performance. Chapter V discusses the development of such a performance-based model that takes into consideration the BCI performance for optimizing the spatial models.

CHAPTER 5

PERFORMANCE-BASED MODEL

The main aim of the dissertation is to better understand brain signals and thus provide the groundwork for improving BCI performance. The Direct-modeling approaches produced an accurate representation of the Archetype s-ERPs, but do not account for BCI performance. All the Direct models optimized the spatial weights by considering the scalp target ERPs for all the channels. Various spatial filtering techniques were also applied on the s-EEG to improve the performance of the direct models, but no significant improvement was observed. Direct models optimized all the time points (0 – 800 ms) of the ERP waveforms. All the time points of EEG do not contain the useful information for P300 classification. Since direct models considered all the time points for the model, this contributed to the low BCI performance.

Based on these results, it is necessary to develop a model that considers the BCI performance (i.e. the output of the BCI classifier). For P300 speller task, step wise linear discriminant analysis (SWLDA) classifier is most commonly used. SWLDA classifier selects certain spatio-temporal features to optimize the performance and rejects the features that do not contain the significant and useful information related to the task. A Performance-based model was developed optimizing the classifier accuracy. This model considers only certain spatio-temporal features selected by the classifier to model s-EEG using i-EEG.

A SWLDA classifier performs a linear transformation of the data. Similarly any i-EEG to s-EEG spatial model based on linear regression also performs a linear transformation.

Two linear transformations can be combined to form another linear transformation. This forms the basis for the Performance-based model.

5.1 PERFORMANCE-BASED MODEL

Using both target and non target ERPs from Archetype s-EEG data, a classifier is trained using SWLDA. This classifier is called s-ERP derived classifier. SWLDA performs a linear transformation of the data to compute the classification accuracy.

The i-EEG to s-EEG spatial model is cascaded with this s-ERP derived classifier. This equivalent cascaded model corresponds to another linear model. The model is optimized using the output of the s-ERP derived classifier. Thus, this model is optimized using the BCI performance criterion i.e. the output of the classifier. Figure 20 shows the block diagram for performance based modeling approach.

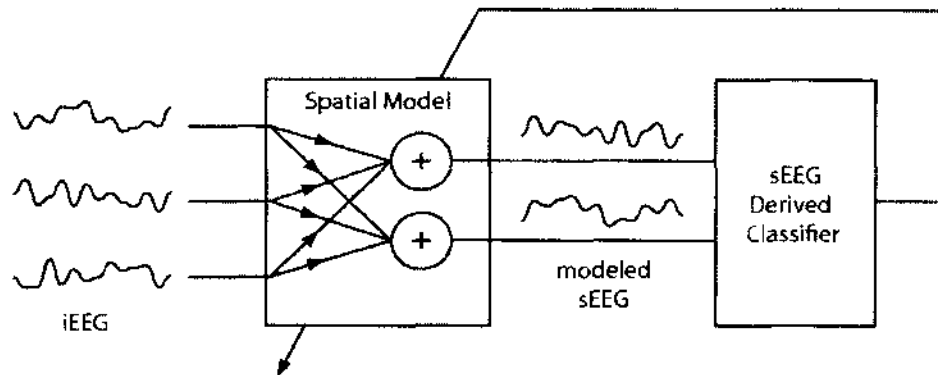


Fig. 20: Performance based modeling approach block diagram. The optimal spatial model is determined by minimizing the output error of the classifier. An ordinary least square linear regression is used to solve for the spatial weights in the linear system created by the cascade of the spatial model with the fixed s-ERP derived linear classifier.

The cascaded linear model follows an ordinary least square linear regression given by Equation 21.

$$y = xb^T \quad (21)$$

where x represents the feature vector corresponding to one flash stimulus of the modeled s-ERPs, generated by the spatial model. This feature vector consists of concatenated spatial and temporal amplitude features of the ERPs corresponding to the flash. b represents the predetermined s-EEG derived classifier weight and y is the instantaneous classifier output [45].

Let Z be the matrix representation of each i-ERP observation of dimension (No. of i-EEG channels \times No. of time samples). If the Z matrix is repeated along the diagonal axis for (number of s-EEG channels) times, keeping all other elements zero, a new matrix \hat{Z} of dimension (s-EEG features \times i-EEG features) is formed as given below:

$$x = \hat{Z}k \quad (22)$$

where k corresponds to the spatial model weights.

$$y = b^T \hat{Z}k$$

Let $R = b^T \hat{Z}$

$$y = Rk \quad (23)$$

Therefore, k can be obtained by using least square linear regression.

$$k = (R^T R)^{-1} R^T y \quad (24)$$

Thus, concatenation of these two linear transformations is equivalent to a linear model. This model is optimized by BCI Performance and thus is named as *Performance-based Model*.

5.1.1 METHODOLOGY

For this model, the first four runs of the i-EEG (both target and non target) session were used to derive the spatial model using stepwise linear regression. The last four runs of the session were used to validate the model. The s-EEG derived classifier selects the specific spatio-temporal features that maximize the performance. Thus, performance based model is optimized using certain spatio-temporal combinations of the features. The model tends to model only these specific features instead of the full ERP waveforms. Since all s-EEG channels were not represented in this model, it is not very meaningful to compute the RMSE between the Modeled and Archetype s-ERPs. Also, it is not informative to compare Archetype and Modeled s-ERPs waveforms.

5.1.2 RESULTS

To validate the performance of this modeling approach, classification performance was evaluated using the optimal s-EEG derived classifier for each subject. The s-EEG derived classifier was trained using Archetype s-EEG ERPs (both target and non target). The second half of Modeled s-EEG ERPs (both target and non target) generated by the spatial

model was used to test the classifier. The score was obtained from the classifier, which can be represented as percentage of correctly classified characters [39].

Table IV gives the classification accuracies obtained for direct and performance-based modeling approaches. The classification accuracies obtained using the optimal linear classifier derived from s-EEG and iEEG are also reported for comparison.

TABLE IV: Classification accuracies for Direct model (with channel selection) and Performance-based model. Columns two and three correspond to optimal linear classifier derived from the s-EEG and iEEG data. The fourth and fifth columns give the results from Performance-based model and Direct model (with channel selection), respectively.

Subject	s-EEG (%)	iEEG(%)	Performance (%)	Direct (with channel selection) (%)
A	100	25	19	19
B	93	100	100	38
C	100	100	100	50
D	100	44	25	19
E	88	81	63	63
F	100	88	81	32

Figure 21 shows the spatial filters from the performance based model. The first column shows the s-EEG SCAs for each subject and also indicates a few of the channels that were included in the s-EEG derived classifier. The second column shows the spatial filter corresponding to the channel with highest SCA that was included in the classifier. The third column corresponds to the spatial filter for the channel that was included in the classifier having lowest SCA. This model is included to illustrate how i-EEG channels contribute to s-EEG channels, that do not appear to contain much discriminative information, but it can help the classifier in conjunction with other channels. The fourth column corresponds to the spatial filter for the channel Cz.

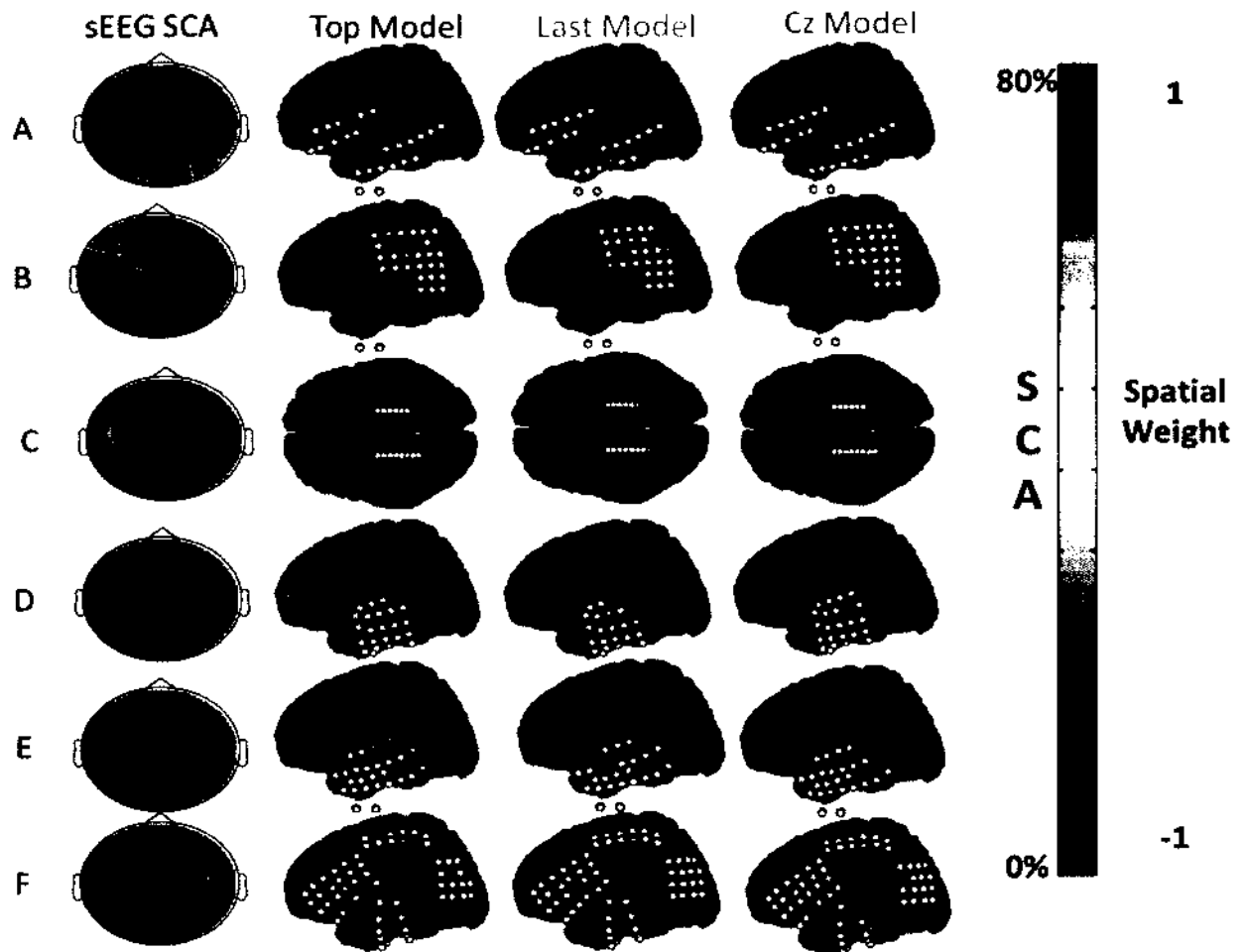


Fig. 21: Spatial models for performance-based modeling. The first column shows the s-EEG SCAs for each subject (A-F). The channels that were included in the s-EEG derived classifier are represented by black dots and the excluded channels as white dots. Additionally, the channel that was included in the s-EEG derived classifier having highest SCA is circled green (Top Model), the channel that was included in the s-EEG derived classifier having lowest SCA is circles in orange (Last Model) and the channel Cz is circled in magenta. The second through fourth columns show the spatial filters corresponding to the Top Model, Last Model and Cz, respectively. The last model is presented to illustrate how the iEEG contributes to the s-EEG channels that do not appear to contain much discriminative information in isolation, but can benefit the classifier in conjunction with other channels.

The performance of four out of six subjects for the performance-based models was comparable or equivalent to the native s-EEG and i-EEG performance. This result indicates that specific s-ERP and i-ERP features are closely related and the model accurately captures this relationship.

5.2 DISCUSSION

Direct models (presented in Chapter III and IV) produced an accurate representation of the Archetype s-ERPs, but did not translate to the best representation for BCI purposes. The Direct models minimized the modeling error of the ERP waveforms in their entirety. Most practical BCI ERP classifiers use only specific combination of spatio-temporal features hence direct models were adversely affected by the irrelevant spatio-temporal features, but the performance is much greater than chance accuracy (3%), thus indicating that these models also capture the key feature relationships but to a lesser extent.

Performance-based models that were designed based on features that are relevant to classification resulted in superior BCI performance, but it is difficult to interpret the resulting spatial models. This is because they model only specific time instances of the response and likely represent more complex spatio-temporal interactions than direct models.

The electrode positions for recording i-EEG are important for BCI performance. Table IV shows that classification performance obtained from modeling is clearly limited by i-EEG BCI performance. Subjects A and D had a huge disparity between s-EEG and i-EEG performance, which could result from suboptimal location of i-EEG electrodes for P300 and perhaps the patients' physical/mental state in the hospital room during the iEEG session.

The spatial filter weights shown in Figure 21, indicate that relatively few i-EEG channels contribute to the estimated waveforms. This is in agreement with SCA obtained for i-EEG as shown in Figure 12. Because these weights tend to occur in small spatially localized groups and in more distant bi-polar pairs, this suggests that inverse spatial models may be effective for estimating the cortical/hippocampal activations. In order to further examine the characteristics of these cortical sources, source localization procedures based on theoretical models are applied and source-based models are developed in Chapter VI.

CHAPTER 6

SOURCE-BASED MODEL

In the previous chapters, both Direct and Performance-based models were developed to understand the relationship between s-EEG and i-EEG. Both models could accurately represent the s-EEG in terms of underlying i-EEG based on different criteria. Performance-based models produced very promising results in terms of BCI performance, but understanding the corresponding spatial models is highly challenging. In order to better understand the underlying brain phenomena to support the empirical results, the location of the sources of brain activity was sought.

6.1 SOURCE LOCALIZATION

Action potentials generated by the voltage-gated ion channels in the neural membranes create current sources in the brain. Much of the membrane current from sources remain in local tissue and form small current loops that may pass through the intercellular membrane and extracellular media. Such local source activity is recorded as local field potentials (LFPs). Some of the cortical current may reach the cortical surface, recorded as i-EEG. Even little gets as far as the scalp in s-EEG. This volume conduction is determined by the geometrical and electrical resistivity of these tissues. Skull tissue has a high resistivity causing currents generated in local cortical regions to spread widely. Thus s-EEG provides a big picture, but little local detail. LFPs provide local details but only sparse spatial coverage. i-EEG provides complimentary and largely independent measures of brain source

activity at different spatial scales [46]. In order to locate these sources, source localization is performed.

Source localization is the process of finding the areas of the brain that are responsible for the recorded brain waves. It comprises of solving two problems, Forward and Inverse problems. Forward problem consists of finding the potentials at the electrodes, for the given set of current dipoles inside the brain. An inverse problem estimates the sources that fit with the given potential distribution at electrodes. An inverse problem can be solved only if the connection between the current sources and electrodes is known. The relationship between the electrodes and current sources is determined by solving the forward problem. Figure 22 gives the schematic representation of the source localization phenomena.

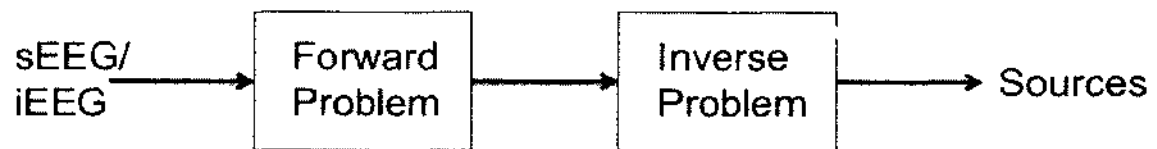


Fig. 22: Schematic representation of the Source Localization

6.1.1 FORWARD PROBLEM

The forward problem describes the propagation of the current from the source to the scalp. Forward problem is solved by using Maxwell's equation and a head model. The head model plays a critical role in source localization because it determines the way intracerebral sources give rise to the recorded potentials. The head model mathematically implements both the electromagnetic and geometrical properties of the solution space.

The forward problem can be expressed as

$$M = AS + E \quad (25)$$

where $M(N_c \times N_t)$ is the electric potential, $S(N_d \times N_t)$ is the current sources at a given time, E is the noise term and $A(N_c \times N_d)$ corresponds to the forward field. Each column of A represents the relationship between the i^{th} dipole and the electrodes. N_c , N_d and N_t refer to the number of electrodes, sources (dipoles) and the number of time samples respectively. Forward field can be estimated accurately if the electrode positions are known precisely.

The purpose of the head model is to find a model that describes the varying conductivity layers in the head. Three head models have been commonly used, namely, spherical head model, boundary element model (BEM) and finite element model (FEM).

The **spherical head model** is used most frequently. It models the head as a set of nested concentric and homogeneous spherical shells. 4-shell spherical head model consists of cortex, CSF, skull and scalp. Standard conductivity values measured in separate studies, are generally used for these different shells. Spherical models can provide appropriate localization in superior regions of the brain where the head shape approximates a sphere [47]. Spherical head model is a very simplified model of human head. In reality, heads are anisotropic, inhomogeneous, and not spherical. Therefore, more realistic head models are needed, to provide a more accurate solution to the forward problem. These models use MRI to extract anatomical information. Surface boundaries for cortex, skull and scalp are extracted from the MRI to build the head model. BEM and FEM are commonly used methods to extract these surfaces from the MRIs.

The **BEM** method assumes homogeneity and isotropy within each region of the head [48]. Different regions of the head (e.g., scalp, skull, CSF, and cortex) are approximated through closed triangle meshes with different conductivity values and dimension. BEM clearly represents an improvement and more realistic model than the spherical head model [49].

The **FEM**, unlike other methods, accounts for the actual head shape and tissue discontinuities. It accommodates anisotropic tissue in the conductivity model of the head volume. FEM allows detailed 3-dimensional information on tissue conductivity for each region. This approach models current flow in an inhomogeneous volume by representing the conductor as a complex assemblage of many equally sized cubes or tetrahedrons. The use of tetrahedrons can accommodate elements that vary in size and thus allow modeling of the head geometry and anisotropy very precisely [50].

In terms of complexity and computational burden, the spherical model represents the simplest, the BEM the intermediate, and the FEM the most complex model. BEM and FEM models better account for individual anatomical differences, providing more realistic head models.

6.1.2 INVERSE PROBLEM

Inverse problem reconstructs the distribution of the electric sources within the brain corresponding to the measured electric potentials. The inverse problem is an under-determined problem and no unique solution can be determined. The reason for non-unique solution is that the space of possible sources distribution has infinite dimension whereas the number of

electrodes is finite. Given the known electrical potential and head volume conductor properties, the distribution of current sources can be computed using various algorithms. There are different localization algorithms that are used to solve the inverse problem. Broadly, these algorithms can be classified into two categories, namely: Dipole source modeling and Distributed source localization.

Dipole source modeling or equivalent current dipole (ECD) modeling assumes that electromagnetic signals are generated by a relatively small number of discrete and focal sources. These sources can be modeled as single, fixed, or moving dipoles. Modeling of each dipole needs six parameters, three location parameters and three orientation parameters. These parameters are estimated iteratively to minimize the difference between the predicted and actual potential measurements [51]. This modeling technique depends on a-priori information regarding the number of dipoles. If the number of dipoles is underestimated, the source model is biased by the missing dipoles. On the other hand, if too many dipoles are specified, then spurious dipoles can get introduced, that may be indiscernible from true dipoles. Also, too many dipoles increase the computational complexity [52]. Various algorithms like Principal Component Analysis (PCA), Multiple Signal Classification (MUSIC) have been developed based on this modeling approach.

Distributed source localization approaches are based on estimation of the brain's electrical activity at each point within a 3-dimensional solution space. Each point, in turn, can be considered a dipole. Unlike equivalent dipole models, these dipoles have fixed positions [53] and sometimes fixed orientations [50], which are determined by anatomical and

physiological constraints implemented within the localization algorithms. Since the number of measurements (electrodes) is typically < 100 , and the number of unknowns (electric sources) is often in the order of 10,000, it is clear that the inverse problem is greatly underdetermined. Regularization methods are needed to limit the range of possible solutions and identify the optimal or most likely solution. Regularization methods can be understood as mathematical representations of the physiological/structural assumptions implemented in a given method. In literature, various regularization methods have been utilized. Some of the most widely used algorithms include minimum norm solution [52], LORETA, and sLORETA [53].

MINIMUM NORM

Minimum Norm (MN) is the most popular 3D linear source localization method. It estimates the 3D brain source distribution with the smaller L2-norm solution vector that matches the measured data. The head model is first mapped onto a 3-dimensional grid, and three mutually perpendicular dipole current sources are placed at each grid point. The goal of the MN approach is to estimate the distribution and strengths of these tens of thousands of dipoles. Among the infinite possible solutions, the MN approach selects the ones that contain the least energy, i.e., minimal overall current density within the brain. Mathematically, the MN solution estimates the 3-dimensional source distribution with the smallest L2-norm solution that fits the actual data. MN does not require any prior information. This method has intrinsic bias that favors superficial sources because sources close to the sensors/electrodes can produce signals with similar strength as strong sources located at deep locations [52].

LOW RESOLUTION ELECTROMAGNETIC TOMOGRAPHY (LORETA)

LORETA [53], a form of Laplacian-weighted MN solution solves the inverse problem by assuming the following

- Neighboring neurons are synchronously activated and display only gradually changing orientations.
- The scalp-recorded signals originate mostly from cortical gray matter.

The first assumption is mathematically implemented by computing the smoothest of all possible activity distributions. The second assumption constrains the solution space to cortical gray matter (and hippocampus), as defined by a standard brain template. Mathematically, LORETA selects the solution with the smoothest spatial distribution by minimizing the Laplacian (i.e., the second spatial derivatives) of the current sources.

STANDARDIZED-LORETA (SLORETA)

In 2002, Pascual-Marqui introduced a variant of the LORETA, s-LORETA, in which localization inferences are based on standardized current density. In s-LORETA a two-step process is followed.

- Current density is estimated using the MN solution.
- The estimated current density is standardized using its expected standard deviation.

Although sLORETA uses a slightly different implementation that considers simultaneously two sources of variations, that is, variations of the actual sources and variations due

to noisy measurements. The localization inference of this algorithm is also based on standardized values of current density estimates. As a result, unlike LORETA, sLORETA does not introduce Laplacian-based spatial smoothness to solve the inverse problem and does not compute current density but rather computes statistical scores [54] [55]. sLORETA is assumed to have zero localization error.

6.2 SOURCE LOCALIZATION FOR INTRACRANIAL EEG

Since i-EEG is recorded in the vicinity of the underlying brain sources and are not influenced by the low conductivity skull, it has higher signal-to-noise ratio as compared to s-EEG. Thus, i-EEG provides better estimation of the sources. Thus, source localization for i-EEG was implemented in this work. The brain sources from i-EEG were estimated by solving the forward and inverse problem. MRI data for only two subjects (C and E) were available. For rest of the subjects (A, B, D and F) average brain MRIs, available in the EMSE Suite, were used to perform source localization.

6.2.1 SOLVING FORWARD PROBLEM FOR I-EEG

Head models were estimated using FEM from patient-specific or average MRI data. The MRI volume was used to identify and segment the boundaries between different tissue types within the head (i.e., scalp, skull, CSF, and cortex). Segmentation was carried out using semi-automated tools (EMSE Suite; Source Signal Imaging Inc., SanDiego, CA). The boundary between white matter and cortical gray matter was identified using a combination of voxel intensity thresholds and a 3D region grow algorithm. The grow algorithm terminated once a boundary of voxels that exceeded a nominated intensity threshold was

detected. This resulted in a 3D mask of all white matter regions up to the border of the inner cortical gray matter boundary. Any points that were incorrectly included in the region were manually edited. Finally, the 3D mask was filled to remove any voxels incorrectly omitted and used to segment the MRI to define the inner cortical gray matter boundary. The inner cortical gray matter boundary is required so that dipoles can be distributed throughout the cortical surface, resulting in a dipole layer that represents potential cortical generators in gray matter. For the i-EEG data, only white and gray matter are needed to generate the head model, since electrodes are implanted on the cortex. Skull and scalp boundaries are not needed. Meshes were then created to approximate the surface of the cortex.

Figure 23 shows the FEM model generated for Subject C. All the three views of the head (axial, coronal, and sagittal) are shown in the figure. Different sections of the cortex, that is, white matter and gray matter are shown as well.

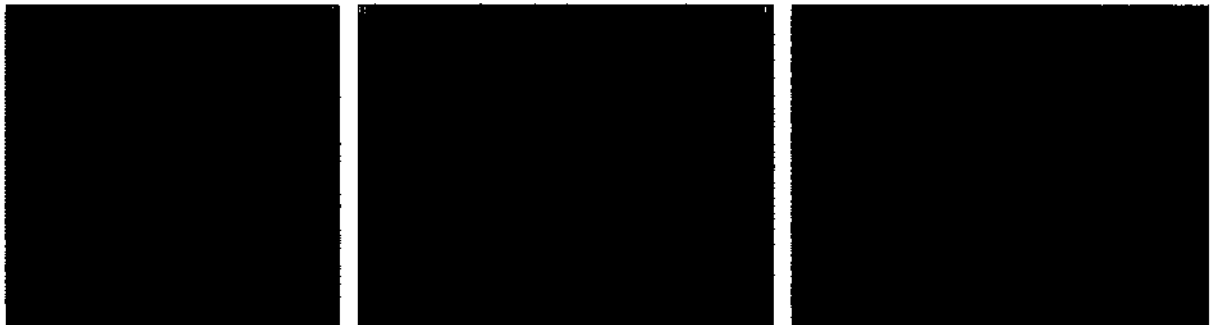


Fig. 23: Axial, Coronal, and Sagittal views of FEM model for Subject C showing the white and gray matter.

The i-EEG electrode locations were co-registered with the MRI surface by visual alignment of the markers. Final adjustment of the co-registration was done using a least square fit algorithm in the EMSE Suite.

6.2.2 SOLVING INVERSE PROBLEM FOR I-EEG

Inverse problem for i-EEG was solved by applying the LORETA algorithm. LORETA algorithm was used because it is the most widely used algorithm for solving the inverse problem. Only the target i-ERPs were used for estimating the brain sources. Common average reference (CAR) filter was applied on all the channels to remove the common artifacts and noise present across all the channels.



Fig. 24: Sources generated from LORETA for Subject C for i-EEG. Yellow circles represent the i-EEG electrode locations.

Figure 24 shows the brain activity observed around the peak of P300 component, obtained by taking the average of i-ERPs across all the channels, for Subject C. For this

subject, the P300 peak was observed around 400 ms. First row of Figure 24 shows the axial, coronal, and sagittal views of the brain activity before the occurrence of the P300 peak (300 ms). The i-EEG electrode locations are shown in yellow circles in the figure. The second row corresponds to the brain activity observed around the P300 peak (400 ms). Third row represents the post P300 brain activity (500 ms). As can be seen from the figure, maximum brain activity is observed around the P300 peak. The activity is observed close to the location of the implanted electrodes in the hippocampus and is highly localized.

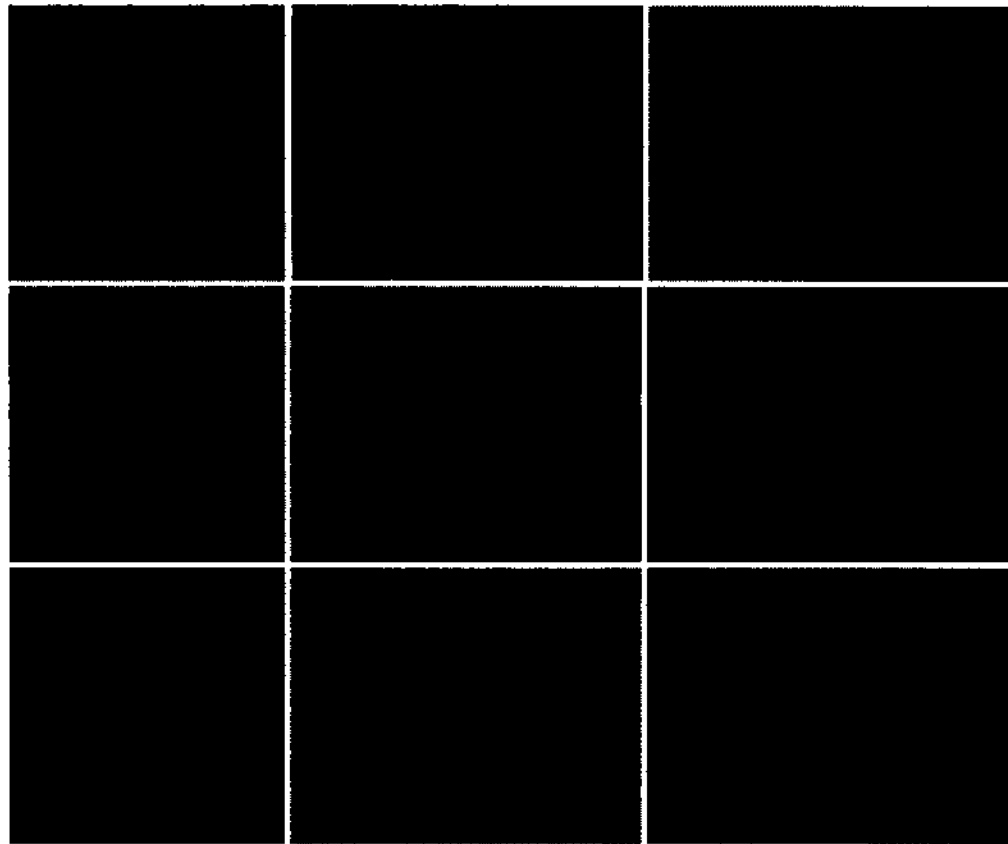


Fig. 25: Sources generated from LORETA for Subject E for i-EEG. Yellow circles represent the i-EEG electrode locations.

Similarly, Figure 25 shows the brain activity observed for the Subject E. The P300 peak was observed around 350 ms for this subject. The first, second and third rows show

the brain activity before, around and post P300 peak. As can be seen from the figure, maximum brain activity is observed around the P300 peak. The activity is observed in the left lateral temporal lobe of the head where electrodes were implanted. For this subject as well, observed brain activity is highly localized.

As stated previously, for subjects C and E, highly localized brain activity was observed. Highly localized activity indicates that very few regions of the brain were active while performing the task.

Figures 26, 27, 28 and 29 correspond to the i-EEG source localization obtained for subjects A, B, D, and F respectively.

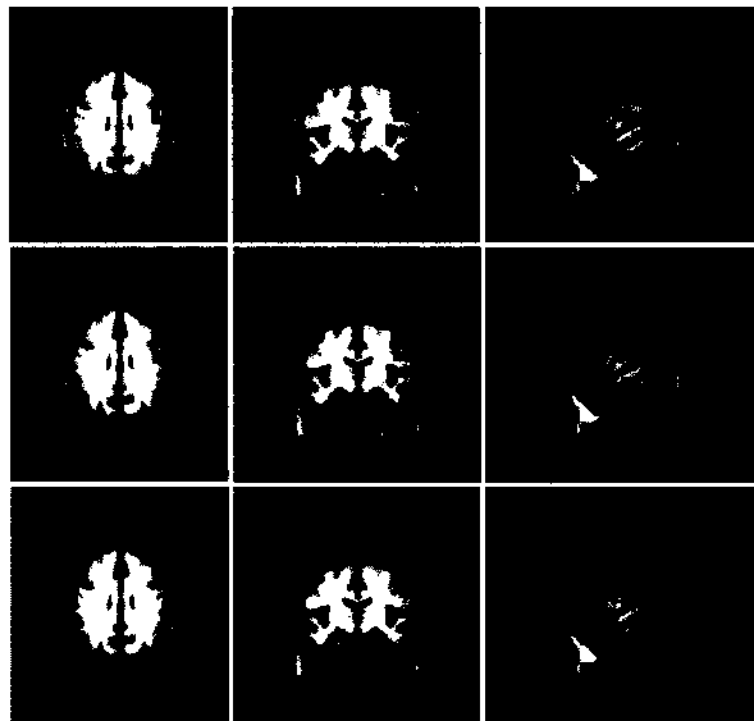


Fig. 26: Sources generated from LORETA for Subject A for i-EEG. Yellow circles represent the i-EEG electrode locations.

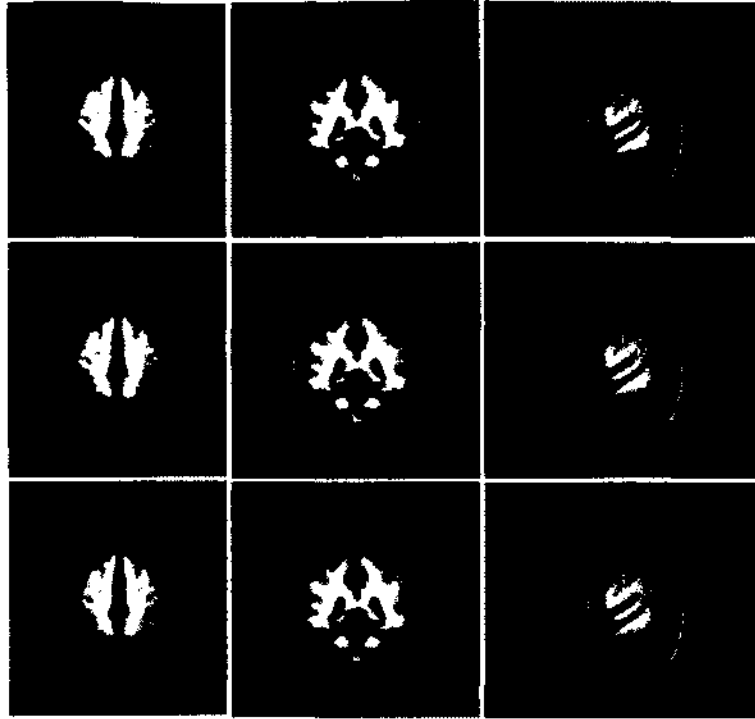


Fig. 27: Sources generated from LORETA for Subject B for i-EEG. Yellow circles represent the i-EEG electrode locations.

Source Localization is an ill-posed problem and does not have a unique solution. For accurate source localization, the subject's actual MRI data are needed. Since average MRI data was used for subjects A, B, D, and F, the sources generated are not very accurate estimates. Furthermore, accurate knowledge of the electrode positions minimizes the localization errors. Because exact electrode positions were not available, the positions were manually determined from the radiographs and verified by the attending neurologist. Thus, average MRIs and inaccurate electrode locations potentially contribute to high localization error.

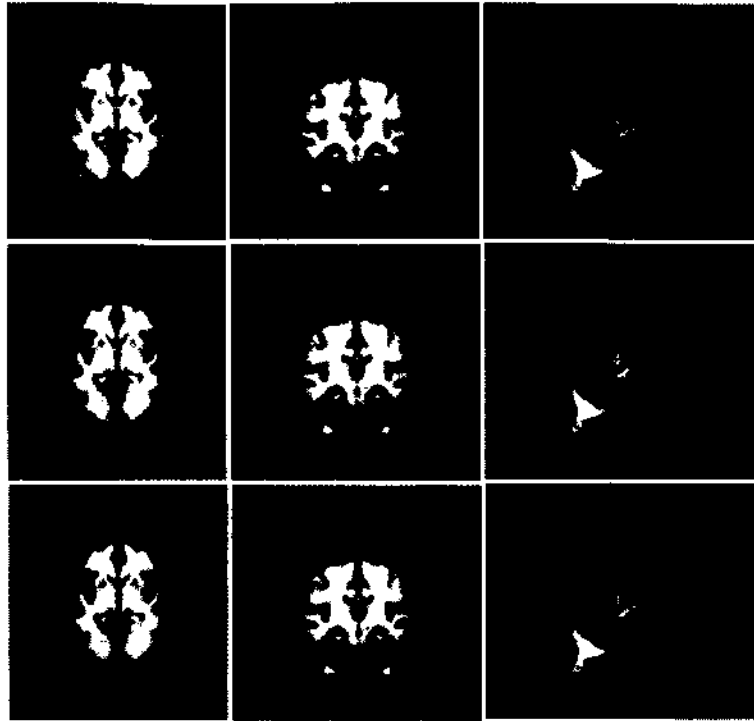


Fig. 28: Sources generated from LORETA for Subject D for i-EEG. Yellow circles represent the i-EEG electrode locations.

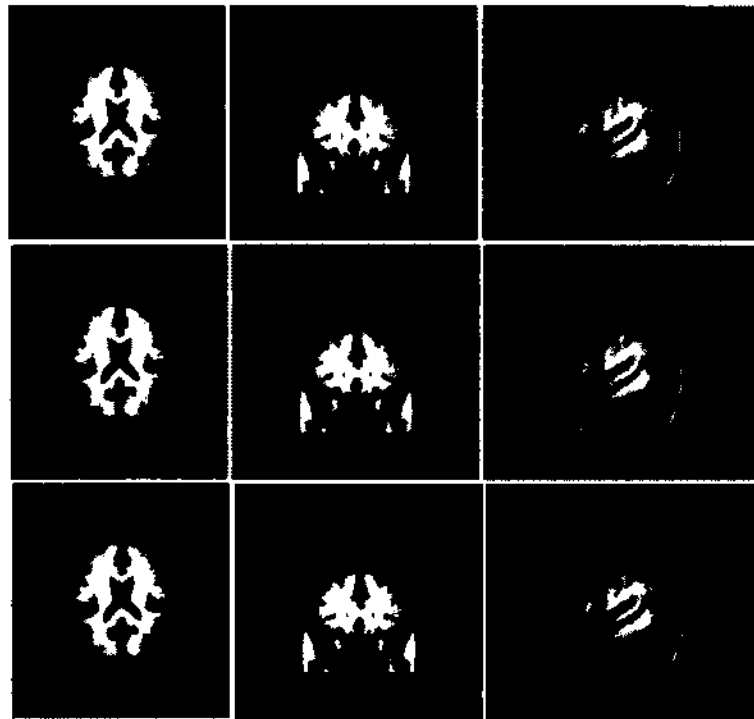


Fig. 29: Sources generated from LORETA for Subject F for i-EEG. Yellow circles represent the i-EEG electrode locations.

6.3 SOURCE-BASED MODEL

To see the effect of attenuation and propagation of electrical signals from their sources to the scalp, a source-based model was developed. The estimated sources from the i-EEG, as obtained in the previous sections can be projected onto the scalp by solving the forward problem. In order to solve this problem, the head model with all the tissues, scalp, inner skull, outer skull, white matter, and gray matter, needs to be constructed. FEM was used to estimate the head model. Following the same procedure as outlined in the previous section 6.2.1, white matter and gray matter boundaries were generated.

An expansion algorithm was used to approximate the inner surface of the skull. Expansion was terminated once all the brain regions, meninges, and CSF were included in the extended mask. The location of the outer skull boundary was then determined in an analogous expansion to a boundary adjacent to but not touching the scalp. The scalp or head boundary was determined after manually removing all extraneous extra-scalp noise in the MRI.

Figure 6.3 shows the FEM head model generated for Subject C. All the three views of the head (axial, coronal and sagittal) are shown in the figure. Different sections of the brain, namely, head (brown), outer skull (blue), inner skull (yellow), gray matter (red) and white matter (green) are shown in Figure 6.3.

Modeled s-ERPs were generated by projecting the estimated sources back on to the scalp using the forward head model. The forward matrix (F_{head}) generated by modeling the complete head was multiplied with the intracranial sources ($I_{sources}$) to generate the spatial weight matrix (W) as given in Equation 26.



Fig. 30: Axial, Coronal, and Sagittal views of the FEM Head model for Subject C. The brown color represents the head, blue corresponds to the outer skull, inner skull is represented by yellow color, red is for the gray matter and green corresponds to the white matter of the head.

$$W = F_{head} \times I_{sources} \quad (26)$$

The Modeled s-ERPs were generated by multiplying the spatial weight matrix with the i-ERPs.

6.3.1 RESULTS AND DISCUSSION

To validate the performance of the developed model, the RMSE between the Archetype and Modeled s-ERPs was computed following the same procedure as discussed in previous chapters. Column 1 of Figure 31 shows the RMSE between the Archetype and Modeled s-ERPs for all the six subjects. Second and fourth columns show the Archetype and Modeled s-ERPs for the first and Cz channels respectively. As can be seen from the plotted ERPs, for most of the subjects, the Modeled and Archetype s-ERPs are closely following each other. The third and Fifth columns correspond to the spatial weights obtained for the first and Cz

channels respectively. These spatial weights indicate that all the channels contribute to the Archetype s-ERPs.

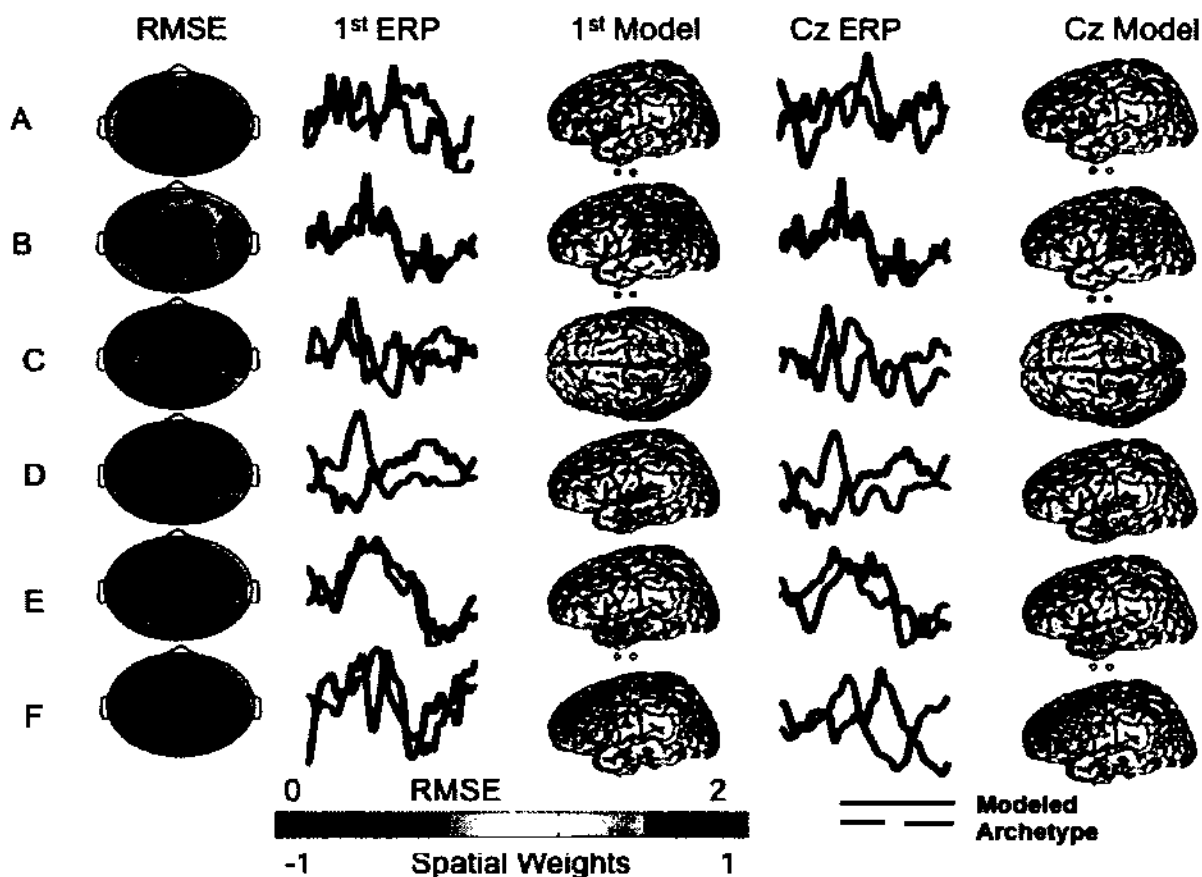


Fig. 31: ERPs and RMSE for Source-based Model. The first column shows the RMSE topographies with the channel corresponding to the lowest RMSE (first channel) circled in purple and channel Cz circled in green. The second and third columns show the Modeled and Archetype s-ERPs and spatial weights for the first channel. The fourth and fifth columns show the Modeled and Archetype s-ERPs and spatial weights for the Cz channel.

For most of the subjects, Modeled s-ERPs accurately represented Archetype s-ERPs for the first channel (lowest RMSE). Subject E, for whom MRI was available, Modeled s-ERPs for the first and Cz channel accurately represent Archetype s-ERPs. The Source-based model for Subject B was developed using average brain MRI and the Modeled and

Archetype s-ERPs are very similar. This may be explained by the fact that Subject B had the electrodes implanted on the left frontal-parietal region of the brain, which plays a key role in P300 activity.

Otherwise, the RMSE obtained for source-based model for most of the subjects is quite high due the aforementioned issues involving average MRI data, electrode localization data, and the lossy behavior of the forward and inverse problem. Joint source localization using both s-EEG and i-EEG can provide better estimates of the brain sources; however, the EMSE Software Suite does not currently support joint source localization.

CHAPTER 7

DISCUSSION, CONTRIBUTIONS, AND FUTURE DIRECTIONS

This dissertation has introduced and evaluated several different empirical models relating scalp and intracranial EEG. These models provide new insights into the relationships between i-EEG and s-EEG, which is envisioned to inspire further studies that employ these findings to improve BCIs. This concluding chapter summarizes the results, contributions, and expounds on several possible directions for future research.

7.1 DISCUSSION

This work is the first to show that key information from scalp ERPs can be accurately modeled using intracranial ERPs that were recorded in separate sessions. This was validated by evaluating offline BCI performance on independent data. While the direct modeling approach can produce accurate representations of the archetype sERPs, this doesn't necessarily translate to representations that maximize BCI performance. This is because the direct models minimize the modeling error of the ERP waveforms in their entirety. However, most practical BCI-ERP classifiers only use a specific combination of spatio-temporal features. Thus, from a BCI performance standpoint, the direct models are likely adversely affected by the irrelevant spatio-temporal features. In contrast, the performance-based models are designed to only account for the features that are relevant to classification. However, the performance-based spatial models are not as clearly interpreted because

the resulting spatial weights may only model a few specific time instances of the response and likely represent more complex spatio-temporal interactions than the direct models.

Consistent with previous work, the results suggest that i-EEG electrode locations are crucial for BCI performance and, in this context, modeling. The BCI performance obtained by the modeling is clearly limited by the native i-EEG BCI performance. The performance disparity between s-EEG and i-EEG for Subjects A and D can be explained by suboptimal i-EEG electrode locations for capturing the desired ERPs, and possibly the patient's physical/mental state in the hospital room during the i-EEG session. Nevertheless, the performance-based modeling results for the other 4 of the 6 subjects was even comparable or equivalent to the native s-EEG and i-EEG performance, indicating that specific s-ERP and i-ERP features are closely related and the models accurately capture these relationships. It should also be noted that the direct models also provide a BCI performance that is much greater than chance, indicating that they also capture key feature relationships, albeit to a lesser extent.

The spatial filter weights for the majority of reliable models indicate that relatively few i-EEG channels contribute to the estimated waveforms, which is expected from the i-EEG SCAs. These weights also tend to occur in small spatially-localized groups or in more distant bi-polar pairs. This localized activity suggests that inverse spatial models may be effective for estimating the cortical/hippocampal activations, which can potentially lead to improved s-EEG-BCI performance.

Only Subjects A and F had significant parietal-lobe overlap, which is a key region for the P300 response. The modeling performance for these subjects was very high using both

metrics. Subject C was the only subject with bilateral hippocampal depth electrodes. It is well known that there are P300 generators in the hippocampus and this subject also exhibited high modeling performance for both metrics. The spatial weights for both models were again concentrated around the right posterior region of the hippocampus. The modeling performance was also high for Subject E, with an unexpected localization in the temporal region. Subject D exhibited similar SCA and modeling localizations, but achieved comparatively poor modeling performance, as did Subject A. It should be noted that the Matrix Speller can evoke different ERP components and spatial distributions compared to the P300 generated by a classical oddball task, including frontal and occipital features. Therefore, while the Speller Matrix can generate ERPs related to the classical P300, the results should not solely be interpreted in the context of the classical P300 response.

Interestingly, the key electrodes for modeling are not always positioned directly under or even spatially adjacent to the respective s-EEG electrodes. This indicates that the responses may be coming from more localized cortical sources and spreading over the scalp via volume conduction. Since the classical P300 response is generally observed centrally (near Cz) in s-EEG, it is expected that both hemispheres are contributing to related s-EEG responses. However, this cannot be easily validated without more complete i-EEG coverage.

7.2 CONTRIBUTIONS

The main contributions of this work are as follows:

- **Direct model:** A Direct model was developed relating the scalp ERPs and intracranial ERPs. This model uses a linear mixture of i-EEG ERPs to estimate s-EEG ERPs by minimizing the error between the temporal waveforms. While several theoretical models exist in literature relating the s-EEG and i-EEG, this is the first empirical model relating the two signals. The resulting models are capable of producing accurate representations of the Archetype s-ERPs depending on the quality of the responses, but have limited capability in terms of improving BCI performance. Very few intracranial electrodes contributed to the scalp electrodes, indicating localized brain activity. Since these models considered all the time points of the ERP waveform, the inclusion of non-significant spatio-temporal features led to poor BCI performance. However, the obtained BCI performance was several standard deviations above chance accuracy.
- **Direct model with spatial filtering:** Spatial filtering based PCA, ICA, and SSA was evaluated as a preprocessing technique for the direct models. These spatial filtering techniques were applied to reduce correlations and unveil the key source components in the data. The direct models with spatial filtering techniques also produced accurate representations of the Archetype s-ERPs. The modeling performance was improved in several cases; however, the improvements were not statistically significant across subjects. This is largely attributed to the fact that these subspace decomposition methods are not optimized based on task-relevant information.

- **Performance-based model:** A novel Performance-based model was developed that optimized the BCI performance. This model considers only significant spatio-temporal features relevant to the classifier. The model produced excellent BCI performance (i.e., comparable to the actual performance) for the subjects that exhibited robust responses. Otherwise, classification accuracy obtained was consistent with the native i-EEG classifier performance, which indicates that the limited classification information present in the i-EEG is being captured by the model. However, the selection of only certain spatio-temporal features makes it difficult to interpret the resulting spatial weights.
- **Source-based model:** To better provide a frame of reference for the empirical results from the earlier chapters, source localization was performed using theoretical conduction models. The sources for i-EEG were estimated using LORETA algorithm and a novel Source-based model was developed that modeled the s-ERPs from the estimated sources of i-EEG. While the resulting models provided reasonable ERP estimations in some instances, the analysis was plagued by errors due to inaccurate/missing imaging data and lossy nature of the operations.

7.3 FUTURE DIRECTIONS

This dissertation provides the initial framework for modeling and better understanding the relationship between scalp and intracranial signals. There are several ways to extend this research, which are briefly discussed below.

- In terms of improving future BCI performance, the Performance-based models models provided the most promising results. It is clear that distinct combinations of spatio-temporal features contain the key discriminative information for BCI applications. However, it is difficult to visualize and interpret the resulting spatio-temporal features to lead to a better understanding of the underlying neural activity. Joint statistical models relating the relevant spatio-temporal features between s-EEG and i-EEG should be developed to give a better understanding of the contribution of each channel and each time point in the models.
- For the source-based model, only i-EEG data were used to estimate the sources. i-EEG electrodes did not cover the complete cortex since they were implanted as per the patients' clinical requirement. Joint source localization using both the scalp and intracranial EEG can give more accurate estimates of the brain sources leading to better source models.
- Because volume conduction is a reasonable assumption, only linear, instantaneous models were developed relating scalp and intracranial EEG. However, since the brain is also a highly-dynamic nonlinear system, it may be worthwhile to employ various dynamic and/or non-linear models such Volterra models and artificial neural networks.
- A logical extension of this work to to evaluate the equivalent linear inverse models, which are essential for estimating the relevant intracranial activity using scalp recordings for practical non-invasive BCIs.

REFERENCES

- [1] <http://www.alsa.org/about-als/>.
- [2] <http://aemf.org/our-research/current-focus/neuromuscular-disorders/>.
- [3] J. R. Wolpaw, N. Birbaumer, D. J. McFarland, G. Pfurtscheller, and T. M. Vaughan. “Brain–computer interfaces for communication and control.” *Clinical neurophysiology*, vol. 113, no. 6, pp. 767–791, 2002.
- [4] J. J. Shih, D. J. Krusienski, and J. R. Wolpaw, “Brain-computer interfaces in medicine,” in *Mayo Clinic Proceedings*, vol. 87, no. 3. Elsevier, 2012, pp. 268–279.
- [5] E. C. Leuthardt, G. Schalk, J. R. Wolpaw, J. G. Ojemann, and D. W. Moran, “A brain–computer interface using electrocorticographic signals in humans,” *Journal of Neural Engineering*, vol. 1, no. 2, p. 63, 2004.
- [6] D. J. Krusienski and J. J. Shih, “Control of a visual keyboard using an electrocorticographic brain–computer interface,” *Neurorehabilitation and Neural Repair*, vol. 25, no. 4, pp. 323–331, 2011.
- [7] J. J. Shih and D. J. Krusienski, “Signals from intraventricular depth electrodes can control a brain–computer interface,” *Journal of Neuroscience Methods*, vol. 203, no. 2, pp. 311–314, 2012.

- [8] G. Schalk and E. C. Leuthardt, "Brain-computer interfaces using electrocorticographic signals," *Biomedical Engineering, IEEE Reviews in*, vol. 4, pp. 140–154, 2011.
- [9] D. J. Krusienski and J. J. Shih, "Spectral components of the p300 speller response in and adjacent to the hippocampus," in *IEEE International Conference on Systems, Man, and Cybernetics (SMC)*,. IEEE, 2012, pp. 274–277.
- [10] A. Furdea, S. Halder, D. Krusienski, D. Bross, F. Nijboer, N. Birbaumer, and A. Kübler, "An auditory oddball (p300) spelling system for brain-computer interfaces," *Psychophysiology*, vol. 46, no. 3, pp. 617–625, 2009.
- [11] M. D. Comerchero and J. Polich, "P3a and p3b from typical auditory and visual stimuli," *Clinical Neurophysiology*, vol. 110, no. 1, pp. 24–30, 1999.
- [12] L. A. Farwell and E. Donchin, "Talking off the top of your head: Toward a mental prosthesis utilizing event-related brain potentials," *Electroencephalography and Clinical Neurophysiology*, vol. 70, no. 6, pp. 510–523, 1988.
- [13] E. Donchin, K. M. Spencer, and R. Wijesinghe, "The mental prosthesis: Assessing the speed of a p300-based brain-computer interface," *Rehabilitation Engineering, IEEE Transactions on*, vol. 8, no. 2, pp. 174–179, 2000.
- [14] D. J. Krusienski, E. W. Sellers, F. Cabestaing, S. Bayoudh, D. J. McFarland, T. M. Vaughan, and J. R. Wolpaw, "A comparison of classification techniques for the p300 speller," *Journal of Neural Engineering*, vol. 3, no. 4, p. 299, 2006.

- [15] G. D. Johnson and D. J. Krusienski, "Ensemble svlda classifiers for the p300 speller," in *Human-Computer Interaction. Novel Interaction Methods and Techniques*. Springer, 2009, pp. 551–557.
- [16] M. Kaper, P. Meinicke, U. Grossekhoefer, T. Lingner, and H. Ritter, "Bci competition 2003-data set iib: support vector machines for the p300 speller paradigm," *Biomedical Engineering, IEEE Transactions on*, vol. 51, no. 6, pp. 1073–1076, 2004.
- [17] E. W. Sellers, D. J. Krusienski, D. J. McFarland, T. M. Vaughan, and J. R. Wolpaw, "A p300 event-related potential brain–computer interface (bci): the effects of matrix size and inter stimulus interval on performance," *Biological Psychology*, vol. 73, no. 3, pp. 242–252, 2006.
- [18] J. Lu, W. Speier, X. Hu, and N. Pouratian, "The effects of stimulus timing features on p300 speller performance," *Clinical Neurophysiology*, vol. 124, no. 2, pp. 306–314, 2013.
- [19] G. Townsend, B. LaPallo, C. Boulay, D. Krusienski, G. Frye, C. Hauser, N. Schwartz, T. Vaughan, J. Wolpaw, and E. Sellers, "A novel p300-based brain–computer interface stimulus presentation paradigm: moving beyond rows and columns," *Clinical Neurophysiology*, vol. 121, no. 7, pp. 1109–1120, 2010.
- [20] L. Acqualagna and B. Blankertz, "Gaze-independent bci-spelling using rapid serial visual presentation(RSVP)," *Clinical Neurophysiology*, vol. 124, no. 5, pp. 901–908, 2013.

- [21] T. Kaufmann, S. Schulz, C. Grünzinger, and A. Kübler, "Flashing characters with famous faces improves erp-based brain–computer interface performance," *Journal of Neural Engineering*, vol. 8, no. 5, p. 056016, 2011.
- [22] E. W. Sellers and E. Donchin, "A p300-based brain–computer interface: initial tests by als patients," *Clinical Neurophysiology*, vol. 117, no. 3, pp. 538–548, 2006.
- [23] F. Nijboer, E. Sellers, J. Mellinger, M. Jordan, T. Matuz, A. Furdea, S. Halder, U. Mochty, D. Krusienski, T. Vaughan *et al.*, "A p300-based brain–computer interface for people with amyotrophic lateral sclerosis," *Clinical Neurophysiology*, vol. 119, no. 8, pp. 1909–1916, 2008.
- [24] E. W. Sellers, T. M. Vaughan, and J. R. Wolpaw, "A brain-computer interface for long-term independent home use," *Amyotrophic Lateral Sclerosis*, vol. 11, no. 5, pp. 449–455, 2010.
- [25] J. N. Mak, D. J. McFarland, T. M. Vaughan, L. M. McCane, P. Z. Tsui, D. J. Zeitlin, E. W. Sellers, and J. R. Wolpaw, "EEG correlates of p300-based brain–computer interface (bci) performance in people with amyotrophic lateral sclerosis," *Journal of Neural Engineering*, vol. 9, no. 2, p. 026014, 2012.
- [26] J. Mak, Y. Arbel, J. Minett, L. McCane, B. Yuksel, D. Ryan, D. Thompson, L. Bianchi, and D. Erdogmus, "Optimizing the p300-based brain–computer interface: current status, limitations and future directions," *Journal of Neural Engineering*, vol. 8, no. 2, p. 025003, 2011.

- [27] P. Brunner, A. L. Ritaccio, J. F. Emrich, H. Bischof, and G. Schalk, "Rapid communication with a p300 matrix speller using electrocorticographic signals (ecog)," *Frontiers in Neuroscience*, vol. 5, 2011.
- [28] D. J. Krusienski and J. J. Shih, "Spectral components of the p300 speller response in electrocorticography," in *5th International IEEE/EMBS Conference on Neural Engineering (NER)*. IEEE, 2011, pp. 282–285.
- [29] M. Akhtari, H. Bryant, A. Mamelak, E. Flynn, L. Heller, J. Shih, M. Mandelkem, A. Matlachov, D. Ranken, E. Best *et al.*, "Conductivities of three-layer live human skull," *Brain Topography*, vol. 14, no. 3, pp. 151–167, 2002.
- [30] S. K. Law and P. L. Nunez, "Quantitative representation of the upper surface of the human head," *Brain Topography*, vol. 3, no. 3, pp. 365–371, 1991.
- [31] P. L. Nunez, *Electric fields of the brain: The neurophysics of EEG*. Oxford University Press, 2006.
- [32] J. Wolpaw and E. W. Wolpaw, *Brain-computer interfaces: Principles and practice*. Oxford University Press, 2012.
- [33] E. Niedermeyer and F. H. L. da Silva, *Electroencephalography: Basic principles, clinical applications, and related fields*. Wolters Kluwer Health, 2005.
- [34] F. Sharbrough, G. Chatrian, R. Lesser, H. Lüders, M. Nuwer, and T. Picton, "American electroencephalographic society guidelines for standard electrode position nomenclature," *J. Clin. Neurophysiol*, vol. 8, no. 2, pp. 200–202, 1991.

- [35] M. Teplan, "Fundamentals of EEG measurement," *Measurement Science Review*, vol. 2, no. 2, pp. 1–11, 2002.
- [36] E. C. Leuthardt, K. J. Miller, G. Schalk, R. P. Rao, and J. G. Ojemann, "Electrocorticography-based brain computer interface-the seattle experience," *Neural Systems and Rehabilitation Engineering, IEEE Transactions on*, vol. 14, no. 2, pp. 194–198, 2006.
- [37] E. Ludowig, C. G. Bien, C. E. Elger, and T. Rosburg, "Two p300 generators in the hippocampal formation," *Hippocampus*, vol. 20, no. 1, pp. 186–195, 2010.
- [38] G. Schalk, D. J. McFarland, T. Hinterberger, N. Birbaumer, and J. R. Wolpaw, "BCI2000: A general-purpose brain-computer interface (BCI) system," *Biomedical Engineering, IEEE Transactions on*, vol. 51, no. 6, pp. 1034–1043, 2004.
- [39] D. J. Krusienski, E. W. Sellers, D. J. McFarland, T. M. Vaughan, and J. R. Wolpaw, "Toward enhanced p300 speller performance," *Journal of Neuroscience Methods*, vol. 167, no. 1, pp. 15–21, 2008.
- [40] D. J. Krusienski and J. J. Shih, "A case study on the relation between electroencephalographic and electrocorticographic event-related potentials," in *Engineering in Medicine and Biology Society (EMBC), 2010 Annual International Conference of the IEEE*. IEEE, 2010, pp. 6019–6022.
- [41] J. Shlens, "A tutorial on principal component analysis," *Systems Neurobiology Laboratory, University of California at San Diego*, vol. 82, 2005.

- [42] P. Comon, "Independent component analysis, a new concept?" *Signal Processing*, vol. 36, no. 3, pp. 287–314, 1994.
- [43] A. Hyvärinen and E. Oja, "Independent component analysis: Algorithms and applications," *Neural Networks*, vol. 13, no. 4, pp. 411–430, 2000.
- [44] P. von Bünau, F. C. Meinecke, and K.-R. Müller, "Stationary subspace analysis," in *Independent Component Analysis and Signal Separation*. Springer, 2009, pp. 1–8.
- [45] K. Kaur, J. J. Shih, and D. J. Krusienski, "Empirical models of scalp-eeG responses using non-concurrent intracranial responses," *Journal of Neural Engineering*, vol. 11, no. 3, p. 035012, 2014.
- [46] M. Dümpelmann, J. Fell, J. Wellmer, H. Urbach, and C. E. Elger, "3d source localization derived from subdural strip and grid electrodes: A simulation study," *Clinical Neurophysiology*, vol. 120, no. 6, pp. 1061–1069, 2009.
- [47] R. Srinivasan, P. L. Nunez, and R. B. Silberstein, "Spatial filtering and neocortical dynamics: Estimates of EEG coherence," *Biomedical Engineering, IEEE Transactions on*, vol. 45, no. 7, pp. 814–826, 1998.
- [48] S. Baillet, J. C. Mosher, and R. M. Leahy, "Electromagnetic brain mapping," *Signal Processing Magazine, IEEE*, vol. 18, no. 6, pp. 14–30, 2001.
- [49] F. Zanow and M. Peters, "Individually shaped volume conductor models of the head in EEG source localisation," *Medical and Biological Engineering and Computing*, vol. 33, no. 4, pp. 582–588, 1995.

- [50] M. Fuchs, M. Wagner, and J. Kastner, "Development of volume conductor and source models to localize epileptic foci," *Journal of Clinical Neurophysiology*, vol. 24, no. 2, pp. 101–119, 2007.
- [51] C. M. Michel, M. M. Murray, G. Lantz, S. Gonzalez, L. Spinelli, and R. Grave de Peralta, "EEG source imaging," *Clinical neurophysiology*, vol. 115, no. 10, pp. 2195–2222, 2004.
- [52] B. He, *Neural engineering*. Springer, 2005, vol. 3.
- [53] R. D. Pascual-Marqui, C. M. Michel, and D. Lehmann, "Low resolution electromagnetic tomography: A new method for localizing electrical activity in the brain," *International Journal of Psychophysiology*, vol. 18, no. 1, pp. 49–65, 1994.
- [54] R. Pascual-Marqui, M. Esslen, K. Kochi, and D. Lehmann, "Functional imaging with low resolution brain electromagnetic tomography (LORETA): review, new comparisons, and new validation," *Japanese Journal of Clinical Neurophysiology*, vol. 30, pp. 81–94, 2002.
- [55] P. Bocquillon, J.-L. Bourriez, E. Palmero-Soler, N. Betrouni, E. Houdayer, P. Derambure, and K. Dujardin, "Use of swloreta to localize the cortical sources of target-and distracter-elicited p300 components," *Clinical Neurophysiology*, vol. 122, no. 10, pp. 1991–2002, 2011.

APPENDIX

The copyright permission for the Figures 4 and 5 is attached below.

From: **Komalpreet Kaur** <komalpreet@gmail.com>
 Subject: Re: Academic Permissions Request Form
 Date: July 17, 2014 at 1:31 PM
 To: Academic Permissions <Academic.permissions@oup.com>

On Jul 4, 2014, at 8:39 AM, Academic Permissions <Academic.permissions@oup.com> wrote:

Dear Komalpreet,

Thank you for your enquiry. You have our permission to use the OUP Material you list in your email below in your dissertation for submission to Old Dominion University.

If at some future date your dissertation is published it will be necessary to re-clear this permission. Please also note that if the material to be used is acknowledged to any other source, you will need to clear permission with the rights holder.

From: no.reply@oup.com [<mailto:no.reply@oup.com>]
 Sent: 03 July 2014 21:54
 To: Academic Permissions
 Subject: Academic Permissions Request Form

O_Q_URL	/uk/academic/rights/permissions/request
A_Z_firstname	Komalpreet
A_Z_lastname	Kaur
B_Z_Company	Old Dominion University
C_Z_Address	ASPEN Lab Old Dominion University 2117 Engineering Systems Building Norfolk
C_Z_zip	23529
D_Z_PhoneNo	757-343-9701
D_Z_country	USA
E_Z_FaxNo	
F_Z_Email	kkaur003@odu.edu
F_Z_VATnumber	
G_Z_TheirTitle	Dissertation: Empirical modeling of asynchronous scalp recorded and intracranial EEG potentials
H_Z_Author	Komalpreet Kaur
H_Z_Publisher	Old Dominion University
I_Z_Covers	Unspecified
I_Z_PrintRunlength	7
I_Z_pubDate	
J_Z_Territory	World

K_Z_Language	English
K_Z_Notes	
L_Z_Media1	illustration
M_Z_Author1	
M_Z_Title1	Brain-Computer Interfaces: Principles and Practice Format
M_Z_editedby1	Jonathan Wolpaw, Elizabeth Winter Wolpaw
N_Z_Material1	Figures 1.5 and 3.6
O_Z_ISBN1	ISBN 10: 0195388852
O_Z_OUPpubDate1	2012
P_Z_Media2	Text
Q_Z_Author2	
Q_Z_Title2	
Q_Z_editedby2	
R_Z_Material2	
S_Z_ISBN2	
S_Z_OUPpubDate2	
T_Z_Media3	Text
U_Z_Author3	
U_Z_Title3	
U_Z_editedby3	
V_Z_ISBN3	
V_Z_Material3	
V_Z_OUPpubDate3	
W_Z_Additional	
subject	
view	submitform

Oxford University Press (UK) Disclaimer

This message is confidential. You should not copy it or disclose its contents to anyone. You may use and apply the information for the intended purpose only. OUP does not accept legal responsibility for the contents of this message. Any views or opinions presented are those of the author only and not of OUP. If this email has come to you in error please delete it, along with any attachments. Please note that OUP may intercept incoming and outgoing email communications.

VITA

Komalpreet Kaur
 Department of Electrical and Computer Engineering
 Old Dominion University
 Norfolk, VA 23529

Komalpreet Kaur received her B.S. degree in Electronics and Communications Engineering from Guru Nanak Dev University, Amritsar, Punjab, in 2003 and her M.S. degree from the PEC University of Technology, Chandigarh, Punjab in 2006. During her Ph.D. studies, she was a research and teaching assistant working in the Advanced Signal Processing in Engineering and Neuroscience (ASPEN) Lab under the supervision of Dr. Dean J. Krusienski. Her research interests include signal processing, neural networks and pattern recognition, image processing and computer vision, wireless and cognitive radio networks.

Publications

- **K. Kaur**, J. J. Shih, D. J. Krusienski. Modeling scalp-electroencephalogram responses using asynchronous intracranial responses, *J. Neural Eng.* 11(3) 035012, 2014.
- **K. Kaur**, J. J. Shih, D. J. Krusienski. Modeling the Electroencephalogram using Intracranial Signals, *Proceedings of the Fifth International Brain-Computer Interface Meeting: Defining the Future*, Pacific Grove, California, June 3-7 2013.
- **K. Kaur**, M. Wadhwa, E. K. Park. Detection and Identification of Seismic P-Waves Using Artificial Neural Networks, *IJCNN 2013*, Dallas, Texas.
- M. Wadhwa, M. Song, C. Xin, **K. Kaur**. An Efficient Algorithm to Optimize Interference and System Capacity in Wireless Cognitive Networks, *ICNC 2013*.
- M. Wadhwa, C. Xin, M. Song, N. Diawara, Y. Zhao, **K. Kaur**. Optimal Spectrum Sharing for Contention-Based Cognitive Radio Wireless Networks, *Wireless Algorithms, Systems and Applications*, (LNCS WASA 2012), Vol. 7405/2012, 187 - 196.
- K. Singh, **K. Kaur**. Image Encryption using Chaotic Maps and DNA Addition Operation and Noise Effects on it, *International Journal of Computer Applications* (0975-8887), Volume 23, No. 6, June 2011.